OPEN ACCESS

Cancer Immunotherapy ARTICLE

Lipid droplets control anti-tumor immunity by depleting Golgi DAG and blocking IFNGR1 surface trafficking

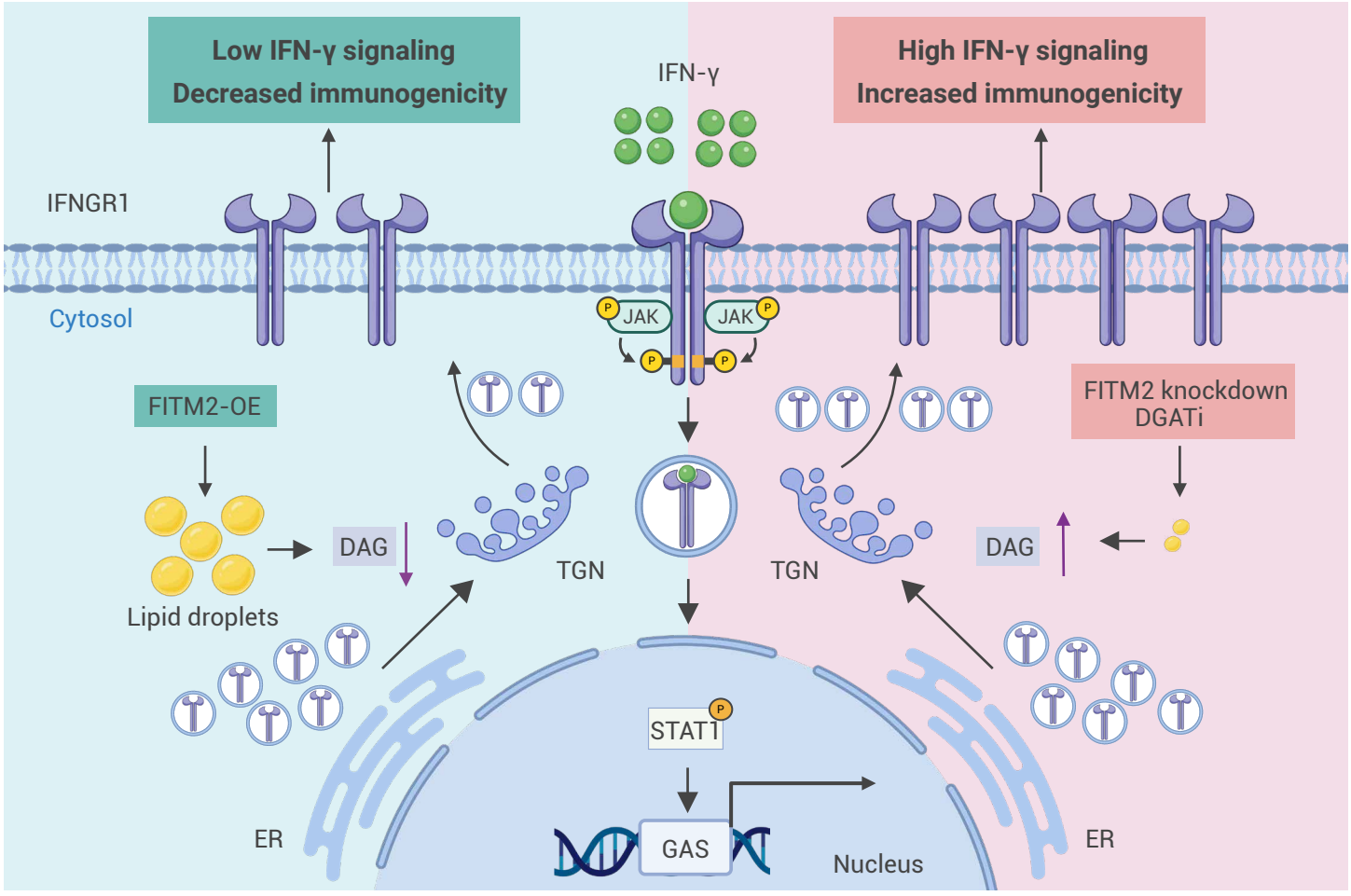
Lingyan Xu,[1,2,4] Yufeng Li,[1,2,4] Xiaofei Li,[1,2,4] Wen Jiang,[1,2] Kai Huang,[1,2] Zhaohui Tang,[3] Xiao Han,[1,2] Weichen Song,[3] Qiang Xu,[3,*] Yanhong Gu,[1,2,*] and Wenjie Guo[3,*]

*Correspondence: guyhphd@163.com (Y.G.); molpharm@163.com (Q.X.); guowj@nju.edu.cn (W.G.)

Received: July 14, 2026; Accepted: October 2, 2026; Published Online: October 2, 2026; https://doi.org/10.59717/j.xinn-oncol.2026.100041

© 2026 The Author(s). This is an open access article under the CC BY license (https://creativecommons.org/licenses/by/4.0/).

GRAPHICAL ABSTRACT



PUBLIC SUMMARY

- Tumor LDs suppress IFNGR1 surface trafficking to drive anti-PD-1 resistance.
- FITM2-driven LD biogenesis preferentially depletes TGN diacylglycerol to impair IFNGR1 trafficking.
- DGAT1 inhibition restores IFNGR1 trafficking and sensitizes CRC to anti-PD-1.
- LDs are organelles that control cytokine receptor trafficking and anti-tumor immunity.

ARTICLE Cancer Immunotherapy

OPEN ACCESS

Lipid droplets control anti-tumor immunity by depleting Golgi DAG and blocking IFNGR1 surface trafficking

Lingyan Xu,[1,2,4] Yufeng Li,[1,2,4] Xiaofei Li,[1,2,4] Wen Jiang,[1,2] Kai Huang,[1,2] Zhaohui Tang,[3] Xiao Han,[1,2] Weichen Song,[3] Qiang Xu,[3,*] Yanhong Gu,[1,2,*] and Wenjie Guo[3,*]

[1]Department of Oncology and Cancer Rehabilitation Centre, The First Affiliated Hospital of Nanjing Medical University, Nanjing 210029, China

[2]Collaborative Innovation Centre for Cancer Personalized Medicine, Nanjing Medical University, Nanjing 210029, China

[3]State Key Laboratory of Pharmaceutical Biotechnology, Department of Gastroenterology, Nanjing Drum Tower Hospital, School of Life Sciences, Nanjing University, Nanjing 210023, China

[4]These anthors contributed equally

*Correspondence: guyhphd@163.com (Y.G.); molpharm@163.com (Q.X.); guowj@nju.edu.cn (W.G.)

Received: July 14, 2026; Accepted: October 2, 2026; Published Online: October 2, 2026; https://doi.org/10.59717/j.xinn-oncol.2026.100041

© 2026 The Author(s). This is an open access article under the CC BY license (https://creativecommons.org/licenses/by/4.0/).

Citation: Xu L., Li Y., Li X., et al. (2026). Lipid droplets control anti-tumor immunity by depleting Golgi DAG and blocking IFNGR1 surface trafficking. *The Innovation Oncology* **1**:100041.

Resistance to anti-PD-1 therapy remains a major challenge in colorectal cancer (CRC), particularly in microsatellite-stable tumors, yet the underlying mechanisms are incompletely understood. Here, we identify tumor lipid droplets (LDs) as a driver of immune evasion and anti-PD-1 resistance. In CRC patients receiving anti-PD-1 therapy, progressive disease correlates with high tumor LD content and reduced plasma membrane IFNGR1. Mechanistically, fat storage-inducing transmembrane protein 2 (FITM2)-driven LD biogenesis preferentially depletes trans-Golgi network (TGN) diacylglycerol (DAG) without altering total cellular DAG or other TGN lipids, thereby impairing IFNGR1 vesicular trafficking to the plasma membrane and attenuating JAK2-STAT1 signaling. Genetic (FITM2 knockdown) or pharmacological (DGAT1 inhibitor A922500) LD reduction restores TGN DAG pools, rescues IFNGR1 surface localization, reactivates IFN-γ signaling, and synergizes with anti-PD-1 therapy in orthotopic CRC models. These findings define LD-driven TGN DAG depletion as a mechanistic link between lipid metabolism and immunotherapy resistance and nominate LD biogenesis targeting as a strategy to overcome anti-PD-1 resistance.

INTRODUCTION

Immunotherapy based on immune checkpoint inhibitors (ICIs) has emerged as a groundbreaking strategy for cancer treatment. In advanced colorectal cancer (CRC), ICIs have received Food and Drug Administration (FDA) approval only for 4-5% of patients with microsatellite instability high (MSI-H) / DNA mismatch repair-deficient (dMMR) molecular profile.[1,2] In contrast, most patients with microsatellite stable (MSS) / DNA mismatch repair-proficient (pMMR) CRC exhibit an immune-excluded and immunosuppressive tumor microenvironment, characterized by low mutational burden and limited availability of neoantigens.[3,4] Despite extensive clinical trials exploring combination therapies, outcomes have largely been disappointing.[4-7]

The clinical application of ICIs is significantly hindered by limited efficacy and unsustainable therapeutic responses, due to various tumor-intrinsic resistance mechanisms.[8-10] These mechanisms include insufficient tumor antigenicity, abnormal interferon signaling, loss of antigen-presenting molecules, and oncogenic pathway activation.[11] Among the key determinants of T-cell-mediated tumor killing is the tumor cell's ability to sense and transduce interferon-γ (IFNγ) stimulation, a process that critically depends on the surface availability of interferon-γ receptor 1 (IFNGR1). Reduced IFNGR1 membrane localization has been linked to impaired IFN-γ signaling, ultimately rendering tumors resistant to checkpoint inhibition.[2] However, the regulatory mechanisms that govern IFNGR1 trafficking to the plasma membrane in CRC cells remain incompletely understood.

Lipid droplets (LDs) are highly dynamic organelles consisting of a neutral lipid core (triglycerides and cholesteryl esters) surrounded by a phospholipid monolayer decorated with specific proteins. These proteins include enzymes for lipid metabolism, members of the perilipin family and proteins with other functions such as membrane trafficking and protein degradation.[12] Traditionally, LDs are known to mitigate lipotoxicity and maintain cellular lipid and energy homeostasis.[12] However, LD accumulation is a hallmark of tumor cells and has been implicated in promoting proliferation, invasion, metastasis, and resistance to chemotherapy and radiotherapy.[13] In CRC, LDs contribute to resistance against 5-fluorouracil and oxaliplatin, partly by reducing immunogenic cell death.[14] Despite these advances, the dynamic metabolic checkpoints linking tumor cell-intrinsic lipid metabolism to immune signaling remain poorly understood. Organelle-to-plasma-membrane lipid flux — the vectorial transfer of lipid intermediates from intracellular compartments to the cell surface — has been largely overlooked as a potential regulatory node in anti-tumor immunity.

Here, by genetically (FITM2 knockdown) or pharmacologically (DGAT1 inhibitor A922500) reducing LD content, we show that LD depletion sensitizes CRC to anti-PD-1 therapy. Mechanistically, LDs restrict IFNGR1 trafficking to the plasma membrane by depleting DAG in the trans-Golgi network (TGN), thereby impairing sustained JAK2-STAT1 signaling. Restoring TGN DAG pools and IFNGR1 surface expression through LD reduction markedly enhances the therapeutic efficacy of anti-PD-1 treatment in CRC.

MATERIALS AND METHODS

Cell lines and culture conditions

LD-high human colon cancer cell line (HT29), LD-low human colon cancer cell line (SW620), human embryonic kidney cell line (HEK293T), and mouse colon cancer cell lines (CT26 and MC38) were purchased from Shanghai Cell Bank of Chinese Academy of Sciences (Shanghai, China). These cells were cultivated in McCoy's 5A, high-glucose DMEM or RPMI-1640 medium supplemented with 10% fetal bovine serum, penicillin and streptomycin under a humidified 5% CO_2 atmosphere at 37 °C in an incubator (Biological Industries, Kibbutz Beit Haemek, Israel). All cell lines were routinely tested for Mycoplasma contamination using the PCR-based MycoBlue Mycoplasma Detector Kit (Vazyme, China) by Genetic Testing Biotechnology (Suzhou, China), and only Mycoplasma-free cells were used in the experiments.

Lentiviral transduction and plasmid transfection

Mouse and human FITM2 short hairpin RNA (shRNA) and luciferase virus were purchased from GeneChem (China), and mouse *Ifngr1* (IFN-γRα) shRNA was purchased from Santa Cruz Biotechnology. For information of the specific shRNA, please refer to the key resource table. Mouse and human colon cancer cell lines were transduced with lentivirus and selected with puromycin or geneticin (G418). The pcDNA-FITM2-HA, pcDNA-PKD-GFP and pcDNA-OSBP-PH-GFP were designed and synthesized by General Biol (China). The plasmids were transfected into cells using Lipofectamine 2000 according to the manufacturer's instructions.

In vivo experiments

Female BALB/c and C57BL/6 mice (6-8 weeks old, 18-20 g), as well as BALB/c nude mice, were obtained from Charles River Laboratories (Beijing, China). The mice were housed in plastic cages at a temperature of 21 ± 2 °C under a 12-hour light/dark cycle and were given free access to pellet food and water. All animal care and experimental procedures adhered to the Guide for the Care and Use of Laboratory Animals. The experimental protocols were approved by the Ethics Committee of Nanjing Medical University, with efforts to reduce animal members and minimize suffering (Nanjing, P.R. China; IACUC-2410055). Mice were randomized to treatment groups, and outcome assessments were performed blinded where feasible.

To assess tumor changes following anti-PD-1 treatment, BALB/c mice with CT26 tumors and C57BL/6 mice with MC38 tumors were randomly assigned to receive either PBS or anti-PD-1 treatment (100 μg, i.p., every 3 days). Tumor tissues were collected for Oil Red O staining.

To examine the impact of FITM2 in anti-PD-1 treatment, CT26 sh*Ctrl* and sh*Fitm2* cells (8×10^5 cells in 100 μL PBS per mouse) were subcutaneously injected into BALB/c mice, respectively. Tumor formation was successfully established in more than 95% of the implanted mice. The mice were assigned to receive either PBS or anti-PD-1 treatment (100 μg, i.p., every 3 days).

To better recapitulate the intestinal microenvironment, an orthotopic transplantation tumor model was used as previously described.[15] To enable longitudinal bioluminescence imaging, all colon cancer cell lines were lentivirally transduced to express firefly luciferase. We first established donor tumors by subcutaneous implantation, excised tumors into small pieces, and then implanted them into the cecal wall of mice under isoflurane anesthesia. The abdominal wall was sutured, and mice received postoperative antibiotic prophylaxis. The orthotopic engraftment rate was approximately 85%, demonstrating the robustness and reproducibility of the tumor implantation model. Mice without detectable bioluminescence at day 3 were excluded. The mice were randomly assigned to receive either PBS or Anti-PD-1 treatment (100 μg, intraperitoneally, every three days). Tumor growth was quantified *in vivo* on an IVIS Spectrum System (PerkinElmer, Waltham, USA) after administering D-luciferin potassium salt via intraperitoneal injection. Photon flux was quantified using identical regions of interest (ROIs) and exposure settings across all groups, allowing direct comparison of radiance values without additional correction. Photon flux values were log10-transformed and longitudinal data were analyzed by two-way repeated-measures ANOVA with Geisser-Greenhouse correction and Sidak's post-hoc test.

To determine whether IFNGR1 mediates the effect of FITM2 on anti-PD-1 efficacy, we constructed CT26 cells with dual knockdown of both *Fitm2* and *Ifngr1*. The cells were injected subcutaneously into BALB/c mice. The mice were then randomly assigned to receive either PBS or anti-PD-1 treatment (100 μg, intraperitoneally, every 3 days). Body weight and tumor volume were regularly monitored.

For further validation of the effect of DGAT1 inhibitor A922500 in anti-PD-1 treatment, the orthotopic transplantation tumor model was constructed. Mice were randomly divided into 4 groups: (1) mice received 100 μL PBS i.p. daily; (2) mice received 3 mg/kg DGAT1 inhibitor by orally daily; (3) mice received 100 μg anti-PD-1 i.p. every 3 days; (4) mice received anti-PD-1 combined with A922500.

The double-blind strategy was rigorously implemented throughout the experiment: investigator A, who was blinded to group allocation, administered all treatments; investigator B, who was also blinded, performed all imaging acquisitions and bioluminescence signal quantifications. Group allocation was concealed from both investigators until all data analyses were finalized. This double-blinding approach effectively minimized potential performance and detection biases. At the study endpoints, mice were euthanized and tumors were excised for histologic analysis and flow cytometry.

Oil red O staining and LD visualization

Frozen tumor tissue sections and cultured cells seeded on slides were stained with Oil Red O solution. Excess stain was removed by three washes with distilled water. Lipid droplets appeared orange-red to bright red, while nuclei were stained blue. Cells were visualized using a phase-contrast microscope (Olympus Corp., Tokyo, Japan).

For live cell imaging, LDs were stained with BODIPY 493/503 (1 μM) for 30 minutes and visualized by confocal microscopy (Carl Zeiss LSM510 Meta or LSM800, 63x/1.4 NA oil). For quantitative analysis, lipid droplets were stained with BODIPY 493/503 (1 μM) detected by flow cytometry.

LDs were identified in patient and xenograft tumor tissues using immunofluorescence with an antibody targeting PLIN2. After antigen retrieval, tissue sections were incubated with the PLIN2 primary antibody, followed by incubation with an appropriate fluorescent secondary antibody. The slides were then mounted and imaged by confocal microscopy.

Human sample collection

Paraffin-embedded tissues from 14 colorectal cancer patients who had previously received immunotherapy were collected from the First Affiliated Hospital of Nanjing Medical University. This study was approved by the Ethics Commission of Jiangsu Province Hospital (2021-SR-160.A1 and 2021-SR-544) and conformed to the International Conference on Harmonization Guidelines for Good Clinical Practice and the provisions of the Declaration of Helsinki. These paraffin sections were used for further immunofluorescence analysis. Written informed consent was obtained from all patients at the time of enrollment.

Immunofluorescence

Following fixation with 4% formaldehyde, permeabilization with saponin, and blocking with 3% bovine serum albumin (BSA), cells and tumor tissue sections were incubated with primary antibodies at 4 °C overnight. Subsequently, species-appropriate fluorescent secondary antibodies were applied. Nuclei were stained with DAPI, and samples were imaged by confocal microscopy (Carl Zeiss LSM510 Meta or LSM800, 63x/1.4 NA oil). Semi-quantitative analysis of specific protein expression (PLIN2, p-STAT1 and IFNGR1) was performed by measuring the mean gray value (Mean) in Fiji. To quantify co-localization of IFNGR1 with organelle markers, and of OSBP-PH-GFP or PKD-GFP with Golgi markers, the Pearson correlation coefficient was calculated using the Coloc2 plugin in Fiji. The Pearson correlation coefficient ranges from +1 for perfect correlation to near 0 for no correlation.[16]

Histological analysis

Hematoxylin-eosin (H&E) staining and immunohistochemistry (IHC) were performed according to the manufacturer's protocols. Following deparaffinization, rehydration, antigen retrieval, and blocking, tissue sections were incubated with primary antibodies at 4 °C overnight, developed with 3,3′-diaminobenzidine (DAB) and counterstained with hematoxylin. Slides were examined under a light microscope (Olympus). The percentage of PCNA-positive cells was quantified using Fiji. For semiquantitative scoring, staining intensity (0: negative; 1: light yellow; 2: light brown; 3: dark brown) and the proportion of positive cells (1: 0–25%; 2: 26–50%; 3: 51–75%; 4: 76–100%) were multiplied to yield an IHC score. Two independent observers blinded to group allocation scored the slides, and discrepancies were resolved by consensus.

Western blot analysis

Whole cells were harvested on ice in cell lysis buffer supplemented with PMSF and protein phosphatase inhibitors. Total protein concentration was determined using the Pierce BCA Protein Assay kit (Thermo Fisher Scientific). Proteins were separated by 10% or 12.5% sodium dodecyl sulfate-polyacrylamide gel electrophoresis (SDS-PAGE) and transferred to polyvinylidene difluoride (PVDF) membranes (Millipore). Membranes were blocked with 3% BSA and then incubated with primary antibodies at 4 °C overnight, followed by incubation with corresponding secondary antibodies for 90-120 minutes at room temperature. Finally, immunoreactive bands were visualized using the LumiGLO chemiluminescent substrate system (KPL, Gaithersburg, Maryland, USA).

Quantitative real-time PCR (RT-qPCR)

According to the manufacturer's instructions, total RNA was extracted using RNAiso Plus and cDNA was synthesized using the FastQuant RT Kit. qPCR analysis was performed using the SYBR Green Universal Master Mix on a CFX96 Real-time system (Bio-Rad).

In vivo tumor competition assay

CT26 sh*Ctrl*-mCherry and sh*Fitm2*-GFP colon cancer cells were mixed 1:1 prior to injection, and 5×10^5 cells per mouse were injected into immune-deficient BALB/c nude mice or BALB/c mice. Tumor-bearing BALB/c mice were treated with either an isotype control antibody or anti-PD-1 on days 1, 3, 6, and 9. Tumors were harvested on day 12 and dissociated into single-cell suspensions. Tumor composition was analyzed by flow cytometry.

Co-culture and lymphocyte-mediated tumor cell killing assay

Spleens were harvested from BALB/c mice or C57BL/6 mice. Spleens were mechanically dissociated, and the cell suspension was passed through a 40 μm cell strainer and centrifuged. Red blood cells were lysed using Tris-NH_4Cl buffer for 5 minutes at room temperature and quenched with excess PBS and

resuspended in RPMI 1640 supplemented with 5 μg/ml Concanavalin A (ConA) overnight.[17] After activation, lymphocytes were co-cultured with sh*Ctrl* or sh*Fitm2* colon cancer cells for 24 hours, in the presence or absence of anti-IFN-γ neutralizing antibody (20 μg/ml). Cell viability was assessed by flow cytometry.

RNA sequencing

Total RNA extraction, library preparation, and RNA sequencing (RNA-seq) were performed by Novogene. Each group comprised three biological replicates, and the RNA-seq data were deposited in the Gene Expression Omnibus (GEO) database. Differentially expressed genes (DEGs) were analyzed using the DEGseq algorithm provided by Novogene. Upregulated genes following FITM2 knockdown were filtered from the DEG list, and a heatmap of DEGs was generated using the heatmap package in R.

Enzyme-linked immunosorbent assay (ELISA)

Colon cancer cells (2×10^5 cells/well) were seeded in the 24-well plate. The cells were treated with IFN-γ (100 ng/ml) for 24 hours, after which the supernatant was collected for cytokine analysis. Cytokine levels of CCL5 and CXCL10 were measured using Mouse CCL5/RANTES ELISA Kit, Mouse CXCL10/IP-10 ELISA Kit, Human CCL5 ELISA Kit and Human CXCL10 ELISA Kit, in accordance with the manufacturer's instructions.

Preparation of tumor-infiltrating lymphocytes

Tumor tissues were cut into approximately 1 mm^3 pieces in the RPMI-1640 medium supplemented with 10% FBS and enzymatically digested with Mouse Tumor Isolation Kit for 30 minutes on a rotor at 37 °C. The dissociated cells were passed through a 70 μm Cell-Strainer (BD) to isolate single cells. After the supernatant was removed, the cells were suspended in Tris-NH_4Cl to lyse red blood cells. After washing twice with PBS, the cell pellets were re-suspended in sorting buffer (PBS supplemented with 1% FBS) for further staining. The single cells prepared above were stained with Zombie NIR to exclude dead cells and TruStain FcX anti-mouse CD16/32 to prevent nonspecific adsorption. To detect IFNGR1 on the membrane of tumor cells, single cells were stained with anti-mouse CD45-BV510, Biotin anti-mouse IFN-γ Rα chain and PE streptavidin, followed by detection via flow cytometry. To assess the changes in the microenvironment, a Cell stimulation cocktail with protein transport inhibitors was added for 6 hours before staining with Fixation/permeabilization Solution Kit.[18] The antibodies used for staining included: anti-mouse CD45-Brilliant Violet 510, anti-mouse CD4-FITC, anti-mouse CD8a-Brilliant Violet 421, anti-mouse IFN-γ-PE, anti-mouse TNF-α-APC and anti-mouse Granzyme B-PE-CY7. Flow cytometry was performed on Attune NxT Flow Cytometer and analyzed using FlowJo software.

Isolation of cytoplasm and membrane fractions

The cytoplasmic and membrane proteins were fractionated using the Mem-PERPlus Membrane Protein Extraction Kit (Thermo Fisher Scientific) according to the instructions. Briefly, harvested cells were incubated with 750 μL of Permeabilization Buffer at 4 °C for 10 minutes. After centrifugation at 16000 g for 15 minutes, the supernatant was collected as the cytoplasmic protein fraction. The pellet was washed several times with PBS, resuspended in 500 μL of Solubilizing Buffer and incubated for 30 minutes. Subsequently, the sample was centrifuged again at 16,000 × g for 15 minutes, and the resulting supernatant was collected as the membrane protein fraction. Both fractions were then subjected to Western blot.

Membrane protein biotinylation and isolation

HT29 shFITM2 and FITM2-OE cells were collected concurrently, with all subsequent steps performed on ice. Cells were washed three times with 10 mL ice-cold PBS, followed by incubation with 10 mL of 20 mM EZ-Link Sulfo-NHS-LC-Biotin (Thermo Scientific) at 4 °C for 30 minutes. After labeling, the cells were washed once with 10 mL of ice-cold TBS (pH 7.4) and twice with ice-cold PBS. Subsequently, the cells were scraped, collected, and centrifuged at 500 × g for 5 minutes at 4 °C. The cell pellet was resuspended in RIPA buffer supplemented with protease inhibitors and lysed on ice for 30 minutes. The lysates were sonicated for 5 minutes and then centrifuged at maximum speed for 10 minutes at 4 °C. The resulting supernatant was incubated with streptavidin-coated magnetic beads on a rotor at 4 °C for 1 hour. The beads were briefly centrifuged, separated using a magnet, and washed three times with 1 mL of PBS. The bound proteins were eluted for subsequent proteomic analysis.

Proteomics

Proteomics was performed by Metware Biotechnology. The total cell lysates from HT29 shFITM2 and FITM2-OE cells, as well as membrane protein samples, were separated using a Vanquish Neo UHPLC liquid chromatography system. Chromatographic separation was carried out under nano-flow conditions, and the eluted peptides were analyzed by data-independent acquisition (DIA) mass spectrometry on an Orbitrap Astral high-resolution mass spectrometer (Thermo Scientific). Raw data were processed using DIA-NN (version 1.8.1) in library-free mode. Spectra were searched against the Homo sapiens proteome database (downloaded from https://www.uniprot.org/ on 24 February 2025). The Match Between Runs (MBR) option was enabled to construct a spectral library directly from the DIA data, which was subsequently used for re-analysis. Identifications were filtered at both protein and precursor levels to achieve a false discovery rate (FDR) of < 1.2%, and the remaining high-confidence results were used for quantitative analysis.

Electron microscopy

Cells were fixed in situ in 2% glutaraldehyde/4% paraformaldehyde (PFA) for 5 minutes at room temperature. The cells were gently scraped and centrifuged. After discarding the fixative, the cells were fixed in the dark for another 30 minutes. The cells were processed for sectioning and electron microscopy by PINUOFEI BIOLOGICAL.

Extraction of TGN and detection of DAG content

The DAG content in total cells was extracted using a Chloroform: methanol (2:1, v/v) mixture. To detect DAG in the TGN, the TGN was first isolated using Minute Golgi Apparatus Enrichment Kit. Briefly, $25\text{-}35\times10^6$ colon cancer cells were collected and washed once with ice-cold PBS. The cell pellet was resuspended in 550 μL of Buffer A and passed through a pre-cooled centrifugal column twice by centrifugation at 16000 g for 30 seconds. After centrifugation twice to remove mitochondria, endoplasmic reticulum, lysosomes, and cytoplasmic membranes, 400 μL of the supernatant was carefully collected. To isolate the Golgi fraction, 400 μL of Buffer B was added to the supernatant. For TGN isolation, 100 μL of Buffer D was subsequently added to the supernatant, and the resulting pellet was collected as the TGN fraction. Finally, DAG content was measured by the DAG ELISA Kit (mlbio).

Quantification and statistical analysis

All experiments were performed in a minimum of three independent biological replicates. Data were shown as the mean ± standard error of the mean (SEM). Statistical analyses were carried out by GraphPad Prism Software (version 9.5.0). Student's t-test, one-way analysis of variance (ANOVA), and two-way ANOVA were used for statistical analyses. *P* values of <0.05 were considered statistically significant.

RESULTS

Lipid droplet burden in colon cancer cells determines anti-PD-1 response

In subcutaneous CT26 and MC38 colon cancer, we observed a significant accumulation of LDs in tumor tissues following anti-PD-1 treatment, as demonstrated by Oil red O staining (Figure 1A). To further explore the clinical relevance of LD accumulation in tumors, we examined LD content by quantifying PLIN2 expression, a well-established LD marker,[19] in tumor samples from CRC patients receiving anti-PD-1 therapy at the First Affiliated Hospital of Nanjing Medical University. Notably, patients with an assessment of stable disease (SD) exhibited significantly fewer LDs compared to those who were assessed as having progressive disease (PD) (Figures 1B-C & Table S1). The findings prompted us to further investigate the role of LDs in modulating the efficacy of anti-PD-1 therapy in CRC.

The number and size of intracellular LDs are regulated by several factors, including nutritional status,[20,21] key regulatory genes involved in LD

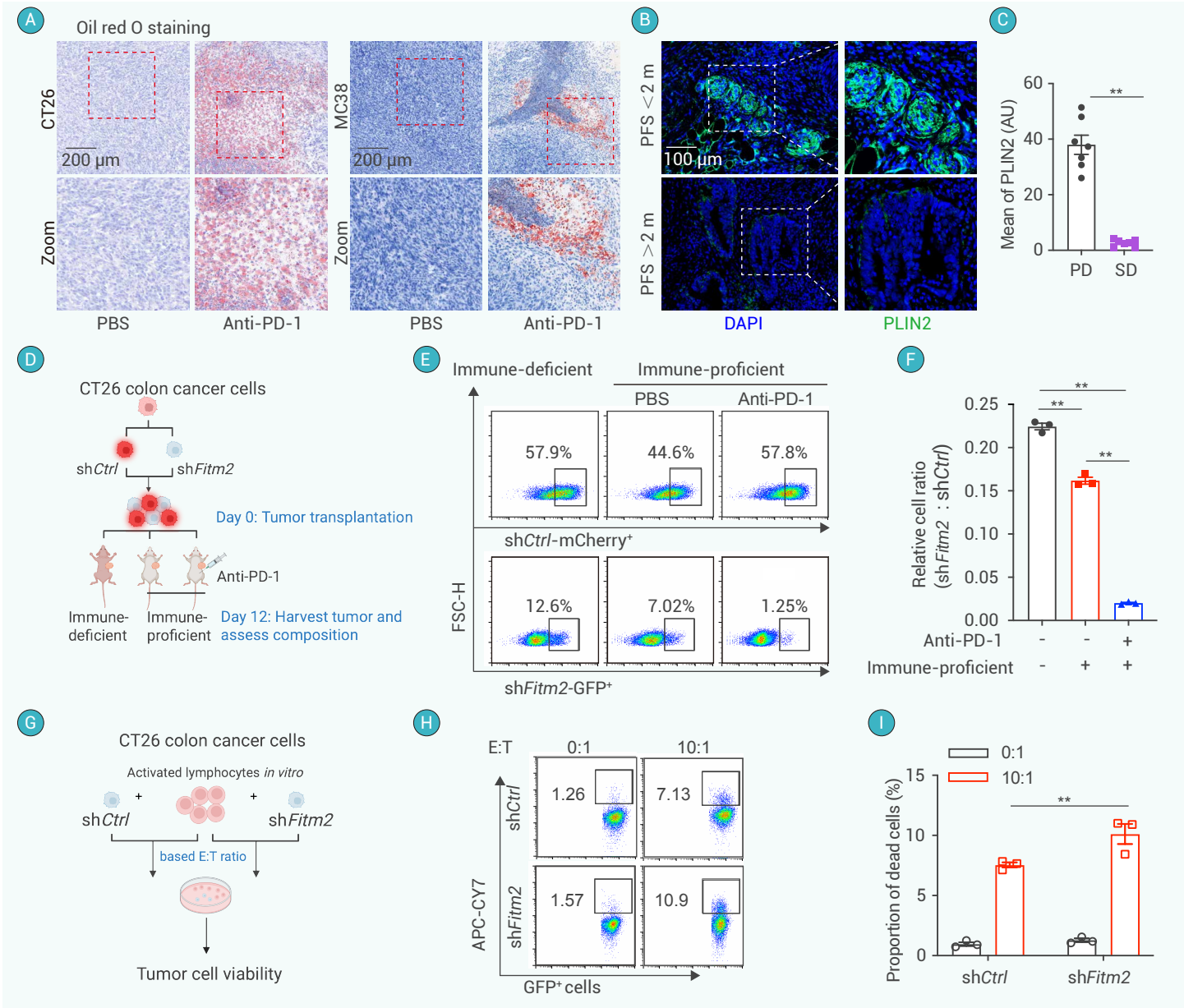


Figure 1. Lipid droplet burden in colon cancer cells determines susceptibility to immune-mediated killing and anti-PD-1 response (A) Representative images of lipid droplets (LDs) stained with Oil Red O in subcutaneous CT26 and MC38 tumors from mice treated with or without anti-PD-1. Scale bar, 200 μm. (B) Representative immunofluorescence images of the LD-associated protein PLIN2 in tumor samples from colorectal patients with different responses to anti-PD-1 therapy, stratified by stable disease (SD) and progressive disease (PD). PLIN2 (green), nuclei (DAPI, blue). Scale bar, 100 μm. (C) Quantification of PLIN2 fluorescence intensity. (D) 1:1 mixture of mCherry-labeled CT26 sh*Ctrl* and GFP-labeled CT26 sh*Fitm2* cells was inoculated into immunodeficient (nude) or immunocompetent (wild-type) mice treated with anti-PD-1. Schematic diagram of the competitive *in vivo* growth assay. (E, F) Flow cytometric analysis of the relative proportions of GFP$^+$ (sh*Fitm2*) and mCherry$^+$ (sh*Ctrl*) tumor cells. (G) CT26 sh*Ctrl* and sh*Fitm2* colon cancer cells were co-cultured with pre-activated mouse spleen lymphocytes *in vitro*. Schematic diagram of the co-culture assay. (H, I) Flow cytometry was used to detect the proportion of dead cells. Data were presented as means ± SEMs. ns, not significant; $^{**}P<0.01$, $^{*}P<0.05$.

formation,[22,23] enzymes associated with phospholipid synthesis[14] and intracellular fatty acid synthesis and catabolism.[24,25] To manipulate LD levels in colon cancer cells, we targeted Fat storage-inducing transmembrane protein 2 (FITM2), a key regulator of the final budding process of LDs from endoplasmic reticulum (ER). Unlike enzymes involved in triglyceride biosynthesis or lipolysis,[23,26] FITM2 influences LD formation without altering overall lipid metabolism, thereby allowing us to dissect LD-dependent mechanisms with minimal confounding effects.

Analysis of the TIMER database (http://timer.cistrome.org/) and a human colon cancer tissue microarray (containing 80 pairs of tumors and matched adjacent tissues) (Table S2) revealed that FITM2 was significantly expressed higher in CRC tissues than adjacent tissues (Figures S1A-B). Furthermore, its expression exhibited a negative correlation with tumor-infiltrating CD8$^+$ T cells in colon cancer (Figures S1C-E). In addition, FITM2 expression was negatively associated with the expression of Interferon-gamma (IFN-γ), CD8A, Granzyme A (GZMA), and perforin (PRF), but not tumor necrosis factor (TNF) (Figure S1F). Furthermore, FITM2 protein expression was significantly higher in tumors from PD patients compared to those from SD patients (Figures S1G-H). The findings prompted us to select FITM2 to regulate the content of LD in colon cancer cells.

We knocked down FITM2 in CT26 and MC38 cells using small hairpin RNAs (shRNAs), with knockdown efficiency confirmed by western blot (Figures S2A & D). FITM2 knockdown significantly reduced both LD content and numbers by flow cytometry and immunofluorescence (IF) (Figures S2B-C & E-F). To assess the impact of FITM2-mediated LD reduction on anti-PD-1 efficacy, we conducted an *in vivo* tumor competition assay. A mixture of GFP-labeled CT26 sh*Fitm2* cells and mCherry-labeled CT26 sh*Ctrl* cells at a 1:1 ratio was co-injected into immune-deficient BALB/c nude mice or immune-proficient BALB/c mice. One day after tumor inoculation, mice were treated with either an isotype control or anti-PD-1 antibody. Tumors

harvested on day 12 showed that under anti-PD-1 treatment, GFP$^+$ CT26 sh*Fitm2* cells were selectively eliminated compared with control (Figures 1D-F & S3A). To further validate these findings, we co-cultured CT26 sh*Ctrl* and sh*Fitm2* cells with pre-activated mouse splenic lymphocytes *in vitro* (Figure 1G). The proportion of dead CT26 sh*Fitm2* colon cancer cells was significantly higher than that of sh*Ctrl* cells (Figures 1H-I & S3B).

In summary, LDs play a crucial role in promoting colon cancer cell survival during anti-PD-1 therapy.

FITM2-driven LD formation reduces surface IFNGR1 without altering total protein

To elucidate how FITM2-regulated LDs in colon cancer cells affect immunotherapy response, we knocked down FITM2 in HT29 (MSS, BRAF-V600E mutant, p53-mutant, LD-high) and SW620 (MSS, KRAS-G12V mutant, p53-mutant, LD-low) human colon cancer cell lines, with knockdown efficiency confirmed by western blot (Figures S2G & I). shFITM2-3 was selected for downstream experiments. Consistent with the role in LD biogenesis, FITM2 knockdown in HT29 and SW620 significantly reduced both the number and content of LDs as assessed by immunofluorescence and flow cytometry with BODIPY 493/503 staining Figures S2H, J & O-P). Conversely, FITM2 overexpression (FITM2-OE) increased intracellular LD accumulation (Figures S2K-N & O-P). Heatmaps of differentially expressed genes indicated that FITM2 knockdown in HT29 colon cancer cells enhanced the expression of genes associated with IFN-γ signaling (Figure S4A). Upon IFN-γ stimulation, phosphorylation of JAK2 (Tyr1007/1008) and STAT1 (Tyr701) was markedly elevated in HT29 and SW620 shFITM2 cells, whereas they were markedly reduced in HT29 and SW620 FITM2-OE cells (Figures S4B-E). RT-qPCR showed an increase in the mRNA expression of CXCL9 and CXCL10 in HT29 and SW620 shFITM2 cells, while FITM2-OE cells displayed reduced transcript levels of these IFN-γ–responsive genes (Figures S4F-G). IF analysis further revealed elevated p-STAT1 levels in HT29 and SW620 shFITM2 cells, and reduced p-STAT1 levels in HT29 and SW620 FITM2-OE cells after IFN-γ stimulation (Figures S4H-I). Additionally, HT29 and SW620 shFITM2 cells secreted higher levels of CCL5 and CXCL10 in the supernatant, whereas FITM2-OE cells secreted lower levels (Figures S4J-K). Together, these results demonstrate that LD depletion via FITM2 knockdown sensitizes colon cancer cells to IFN-γ stimulation by activating the JAK2–STAT1 pathway, highlighting a key role of LDs in restraining IFN-γ signaling and influencing immunotherapy responsiveness.

Although several membrane proteins showed altered abundance in the surface proteome, RNA-seq pathway enrichment analysis specifically converged on IFN-γ signaling as the dominant functional vulnerability (Figure S4A), guiding our subsequent focus on the IFNGR1-JAK2-STAT1 axis. Binding of IFN-γ to its receptor IFNGR1 initiates downstream signal transduction, and increased IFNGR1 abundance on the plasma membrane heightens IFN-γ-mediated signaling.[27] To investigate the upstream components of the IFN-γ signaling pathway, we examined IFNGR1 expression in colon cancer cells with varying FITM2 levels. Flow cytometry analysis revealed that HT29 and SW620 shFITM2 cells exhibited significantly higher IFNGR1 levels on the plasma membrane, whereas these FITM2-OE cells showed significantly lower levels (Figures 2A-D). These findings were further supported by western blot analysis of membrane and cytosolic protein fractions, which confirmed increased membrane localization of IFNGR1 in HT29 and SW620 shFITM2 cells and decreased localization in those FITM2-OE cells (Figures 2E-H).

To ensure experimental consistency, we established HT29 shFITM2 and FITM2-OE cell lines from the same parental batch of HT29 cells. Then, we performed parallel proteomic analyses on whole-cell and plasma membrane proteins isolated from HT29 shFITM2 and FITM2-OE colon cancer cells (Figure 2I). In the whole-cell proteome, FITM2 expression was significantly decreased in shFITM2 cells, confirming successful genetic manipulation (Figure 2J). Proteomic profiling of membrane fractions revealed a marked increase in IFNGR1 abundance in FITM2-silenced cells, whereas no substantial difference was detected in the total cellular proteome (Figures 2K-L). Importantly, modulation of FITM2 expression did not alter the mRNA levels of IFNGR1 or IFNGR2 in either human or mouse colon cancer cells (Figure S5). In addition, the cycloheximide (CHX) chase assay further revealed that FITM2 does not affect IFNGR1 protein stability in HT29 and SW620 cells (Figure S6). Clinically, in the CRC patient cohort receiving anti-PD-1 therapy described above, higher IFNGR1 expression on the plasma membrane was positively correlated with SD (Figure 2M). The clinical data underscore the relevance of IFNGR1 membrane localization to immunotherapy efficacy.

Therefore, FITM2-regulated LDs in colon cancer cells attenuate immunotherapy response by reducing surface IFNGR1 expression without altering total protein levels, thereby inhibiting downstream IFN-γ signaling.

LD biogenesis preferentially depletes TGN DAG, blocking IFNGR1 Golgi export

To delineate the determinants of IFNGR1 surface abundance, we examined its synthesis, intracellular trafficking and plasma membrane localization. Upon IFN-γ stimulation, IFNGR1 in both HT29 and SW620 cells underwent rapid internalization and degradation within 5 minutes, followed by resynthesis (Figure S7). Notably, HT29 and SW620 shFITM2 cells displayed increased IFNGR1 expressed on the plasma membrane in 4 hours post-stimulation, whereas trafficking was reduced in FITM2-OE cells (Figures 3A-E). These observations indicate that FITM2 levels modulate IFNGR1 translocation to the plasma membrane.

Transmembrane proteins such as IFNGR1 are synthesized in the endoplasmic reticulum (ER) and transported through the Golgi apparatus for complex glycosylation.[28] Whole-cell proteome indicates that FITM2 did not alter the abundance of vesicle secretion or transport-related proteins (Table S3). Co-localization of IFNGR1 with organelle markers in HT29 and SW620 cells demonstrated its association with Golgi apparatus (Giantin, TGN46, GM130), ER (calnexin), lysosome (LAMP1) and early endosome (EEA1), but not with transferrin receptor 1(TFRC), Rab11, or LDs (Figures 3F-I & S8A-B). Interestingly, we did not detect colocalization of LDs with the Golgi apparatus (Figures S8C-D), contrary to previous reports.[29,30]

We next focused on the trans-Golgi network (TGN), a central sorting hub in the secretory pathway that directs newly synthesized proteins to their subcellular destinations and receives recycled molecules from the endocytic compartment.[31] To assess the impact of FITM2 on Golgi morphology, we analyzed HT29 and SW620 colon cancer cells with different FITM2 expression levels by transmission electron microscopy. In shFITM2 cells, the Golgi apparatus exhibited intact, tightly stacked saccules with dense surrounding vesicles, whereas FITM2-OE cells showed smaller, disorganized and swollen Golgi structures (Figures 3J-K). Previous studies have highlighted the importance of DAG levels in the Golgi apparatus for protein transport to the plasma membrane.[32] Using PKD-GFP as an indirect reporter of DAG content, we observed that PKD-GFP localized to the TGN in HEK293T vector cells but was diffusely cytosolic in HEK293T FITM2-OE cells, indicating reduced TGN DAG levels (Figures 3L, S9A & C). To determine whether FITM2 specifically affects DAG levels in the Golgi apparatus without perturbing other lipids, we examined PI(4)P indirectly using the Pleckstrin Homology (PH) domain of oxysterol-binding protein (OSBP) fused to GFP. As shown, OSBP-PH-GFP localized to the TGN in HEK 293T vector and FITM2-OE cells, confirming that FITM2 specifically alters DAG levels without affecting PI(4)P (Figures 3M, S9B & D). Direct ELISA measurement of DAG content in HT29 and SW620 cells revealed that shFITM2 cells had elevated DAG in the TGN, whereas FITM2-overexpressing cells showed decreased TGN DAG, without changes in total cellular DAG levels (Figures 3N-O). Importantly, treatment of FITM2-OE cells with the DGAT1 inhibitor A922500 restored IFNGR1 plasma membrane localization, providing functional evidence of DAG-mediated trafficking regulation (Figures 3P-Q).

Collectively, FITM2-driven LD formation depletes DAG from the TGN without detectably altering PI(4)P or total cellular DAG, impairing IFNGR1 trafficking to the plasma membrane, whereas reducing LD content through FITM2 knockdown replenishes TGN DAG and facilitates IFNGR1 surface delivery.

FITM2 knockdown restores IFNGR1 surface expression and enhances anti-PD-1 efficacy

To further investigate whether FITM2-mediated reduction of LDs in colon cancer cells enhances tumor susceptibility to antitumor immunity, we found that FITM2 knockdown resulted in a tumor growth inhibition (TGI) rate of 25.6%, which was further increased to 58.9% when combined with anti-PD-1

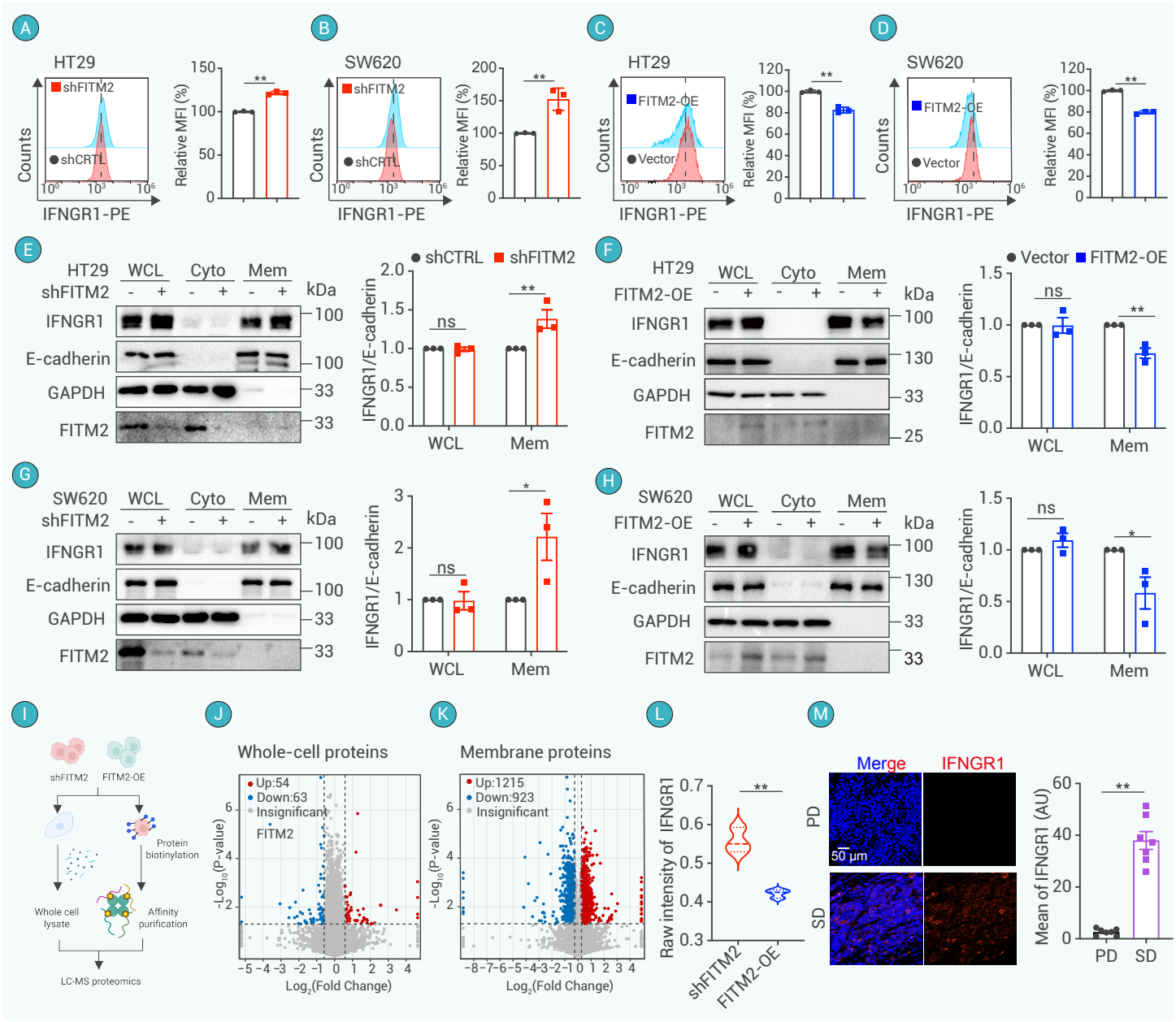


Figure 2. FITM2-driven lipid droplets restrict IFNGR1 trafficking to the plasma membrane, reducing surface IFNGR1 without affecting total protein abundance (A-D) Flow cytometric analysis of IFNGR1 surface expression in (A) HT29 and (B) SW620 cells following FITM2 knockdown (shFITM2), and in (C) HT29 and (D) SW620 cells following FITM2 overexpression (FITM2-OE). (E-H) Western blot analysis of IFNGR1 in subcellular fractions from (E) HT29 shCTRL/shFITM2, (F) HT29 vector/FITM2-OE, (G) SW620 shCTRL/shFITM2, and (H) SW620 vector/FITM2-OE cells. The membrane-to-cytosol ratio of IFNGR1 was quantified relative to the membrane marker E-cadherin. WCL, whole cell lysate; Cyto, cytoplasm; MEM, membrane. (I-L) Quantitative cell surface proteomics. (I) Schematic of the cell surface biotinylation and LC-MS/MS workflow in HT29 shFITM2 and FITM2-OE cells. (J) Log2-transformed fold change of whole-cell proteome. (K) Log2-transformed fold change of the surface proteome (biotinylated fraction). (L) IFNGR1 abundance in the surface proteome. (M) Representative immunofluorescence images of IFNGR1 and PLIN2 in tumor tissues from colorectal patients stratified by response to anti-PD-1 therapy. IFNGR1 (red), nuclei (DAPI, blue). Scale bar, 50 μm. Data were presented as means ± SEMs. ns, not significant; $^{**}P<0.01$, $^{*}P<0.05$.

treatment in the subcutaneous tumor model of CT26 colon cancer (Figures S10A-D). To more closely recapitulate the intestinal microenvironment, we established orthotopic tumor models and achieved consistent therapeutic effects (Figures 4A-D & S11A-D). These results demonstrate that FITM2 knockdown not only suppresses tumor growth but also enhances the efficacy of anti-PD-1 immunotherapy in immunocompetent mice. Histological analysis (H&E staining) and immunohistochemistry (IHC) for PCNA corroborated these findings (Figures 4E, S10E & S11E). By assessing PLIN2 expression, we confirmed reduced LD content in FITM2-deficient tumors (Figures 4F, S10F & S11F). In line with the proposed mechanism, flow cytometry revealed elevated IFNGR1 expression on the tumor cell plasma membrane (Figures 4G, S10G, S11G & S12A). Additionally, the combination of FITM2 knockdown with anti-PD-1 treatment led to an increased proportion of both $CD8^+$ T and $CD4^+$ T cells (Figures 4H-I, S11H-I & S12B). Notably, the proportion of $CD8^+$ T cells secreting effector molecules, including IFN-γ, TNF-α, and GZMB, reached the highest level with this combination regimen (Figure 4J-L , S11J-L & S12B). Furthermore, IHC staining showed that FITM2 knockdown combined with anti-PD-1 therapy significantly upregulated the expression of p-JAK2 and p-STAT1, suggesting robust activation of the IFN-γ-JAK2-STAT1 signaling pathway (Figures 4M-N & S11M-N).

Collectively, these data demonstrate that FITM2 knockdown enhances antitumor immunity and improves anti-PD-1 therapeutic efficacy by reducing LD accumulation, promoting IFNGR1 surface expression, and activating the IFN-γ/JAK2/STAT1 signaling axis. The observation of distinct growth phenotypes exclusively in immunocompetent mice establishes FITM2 as an immune-dependent regulator, consistent with the proposed mechanism whereby FITM2 modulates immune-mediated tumor responses without directly affecting cancer cell proliferation.

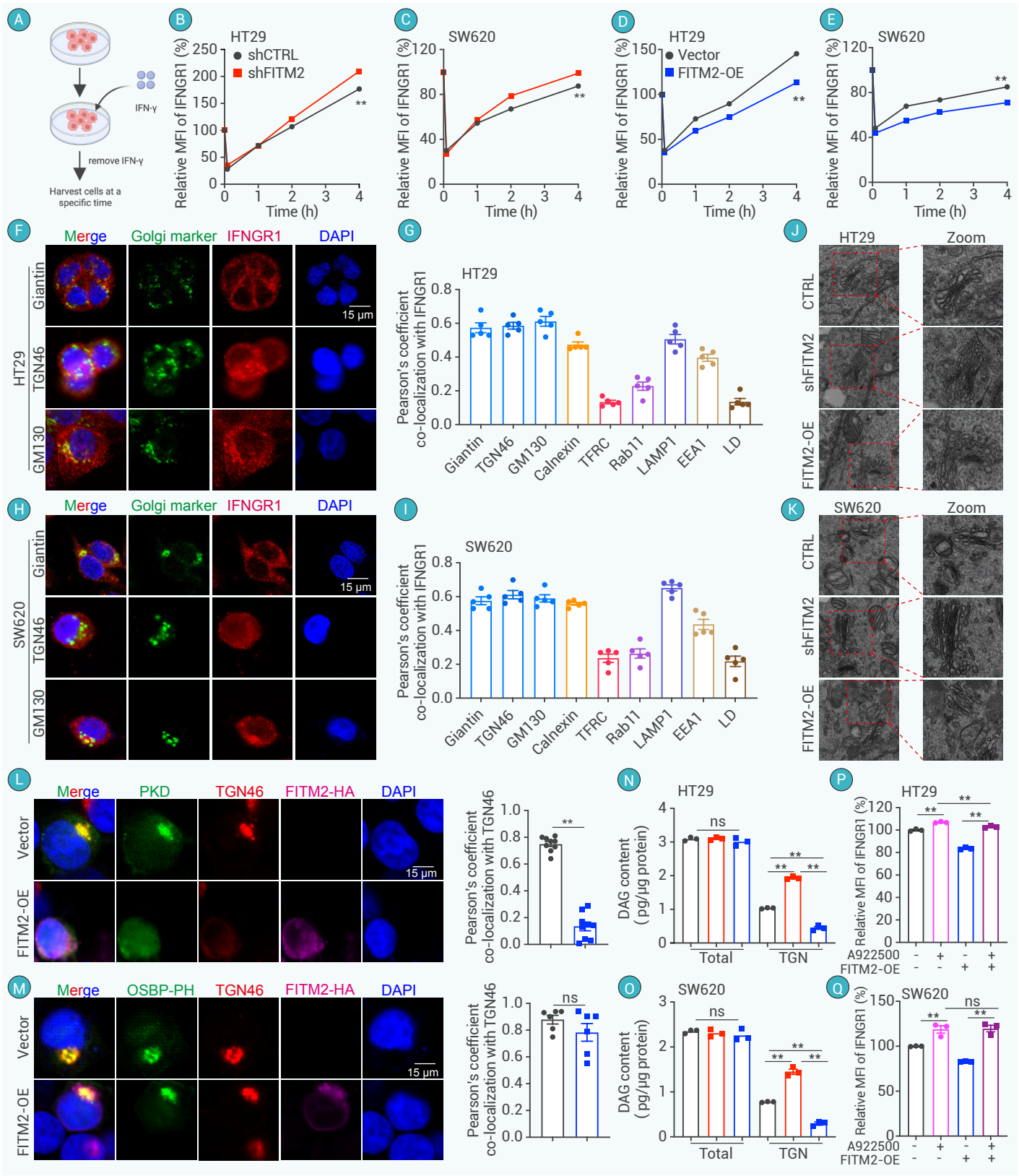


Figure 3. Lipid droplet biogenesis selectively depletes TGN DAG, blocking IFNGR1 export from the Golgi to the plasma membrane (A) Diagram of *in vitro* IFN-γ stimulation of tumor cells. (B, C) Surface IFNGR1 levels, measured by flow cytometry, in (B) HT29 and (C) SW620 colon cancer cells following FITM2 knockdown (shFITM2) versus control (shCTRL) at the indicated times after IFN-γ stimulation. Relative MFI was shown. (D, E) Surface IFNGR1 levels in (D) HT29 and (E) SW620 cells following FITM2 overexpression (FITM2-OE) versus empty vector control at the indicated times after IFN-γ stimulation. Relative MFI was shown. (F) Representative confocal microscopy images of HT29 cells co-stained for IFNGR1 and the Golgi apparatus markers Giantin, TGN46, or GM130 (F). Scale bar: 15 μm. (G) Quantification of Pearson's correlation coefficients for IFNGR1 colocalization with each marker. (H, I) Representative confocal microscopy images (H) and quantification (I) of IFNGR1 colocalization with Golgi markers in SW620 cells. Scale bar: 15 μm. (J, K) Transmission electron micrographs of the Golgi region in (J) HT29 and (K) SW620 control, shFITM2, and FITM2-OE cells. Scale bar: 0.5 μm. (L, M) Colocalization analysis of the DAG biosensor (L) GFP-PKD and PI(4)P biosensor (M) OSBP-PH-GFP with the TGN marker TGN46 in HEK293T control and FITM2-OE cells. Pearson's correlation coefficients were calculated. Scale bar: 15 μm. (N, O) Measurement of cellular DAG content in total cell lysates and TGN fractions from (N) HT29 and (O) SW620 control, shFITM2, and FITM2-OE cells. (P, Q) Surface IFNGR1 levels (MFI) on (P) HT29 and (Q) SW620 FITM2-OE and control cells, treated with or without the DGAT1 inhibitor A922500. Data were presented as means ± SEMs. ns, not significant; $^{**}P<0.01$, $^{*}P<0.05$.

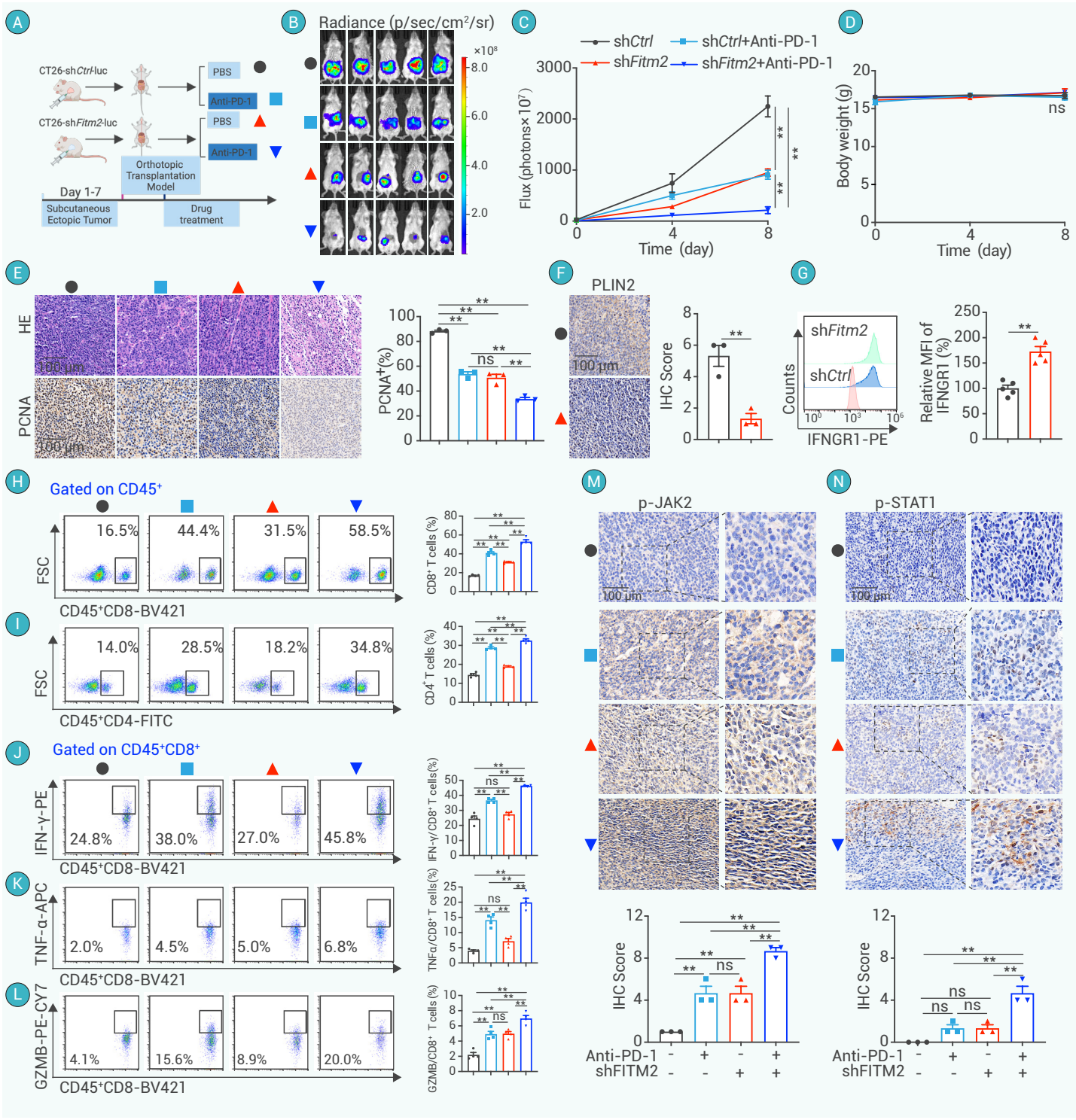


Figure 4. Reducing lipid droplets via FITM2 knockdown restores IFNGR1 surface expression and enhances anti-PD-1 efficacy in orthotopic colorectal cancer (A) Schematic diagram of the experimental timeline. (B) Representative bioluminescence images of orthotopic tumors. (C) Quantification of tumor burden from bioluminescence data. (D) Mouse body weight curves throughout the study. (E) Representative images of tumor sections stained with H&E and for the proliferation marker PCNA. Scale bar, 100 μm. (F) Immunohistochemistry (IHC) for PLIN2 in tumor tissues. Scale bar, 100 μm. (G) Flow cytometric analysis of IFNGR1 surface expression on CD45⁻ tumor cells isolated from sh*Ctrl* and sh*Fitm2* tumors. (H, I) Proportion of tumor-infiltrating lymphocytes among CD45⁺ leukocytes: (H) CD8⁺ T cells and (I) CD4⁺ T cells. (J-L) Flow cytometric analysis of cytokine production in tumor-infiltrating CD8⁺ T cells: (J) IFN-γ, (K) TNF-α, and (L) Granzyme B (GZMB). (M, N) IHC analysis of key signaling molecules in tumor tissues: (M) p-JAK2 and (N) p-STAT1. Scale bar, 100 μm. Data were presented as means ± SEMs. ns, not significant; $^{**}P$ <0.01, $^{*}P$ <0.05.

IFNGR1 surface expression is essential for FITM2-knockdown-mediated sensitization to anti-PD-1

To assess the dependency of FITM2 function on the IFN-γ-JAK2-STAT1 signaling pathway, we co-cultured sh*Ctrl* and sh*Fitm2* cells from both CT26 cell lines with pre-activated mouse splenic lymphocytes *in vitro*, with or without anti-IFN-γ. Notably, FITM2 knockdown cells exhibited increased susceptibility to lymphocyte-mediated killing, which was abrogated by IFN-γ neutralization (Figures 5A-C). For further *in vivo* experiments, we engineered IFNGR1-knockdown (sh*Ifngr1*) mouse colon cancer cells and confirmed this by western blot (Figures 5D & L). IFNGR1 knockdown compromised the therapeutic effect of anti-PD-1 and abrogated the sensitization effect of FITM2 knockdown in CT26 colon cancer models (Figures 5E-H). Consistently, IHC analysis confirmed that IFNGR1 knockdown suppressed the activation of IFN-γ-JAK2-STAT1 signaling by FITM2 knockdown and anti-PD-1 treatment

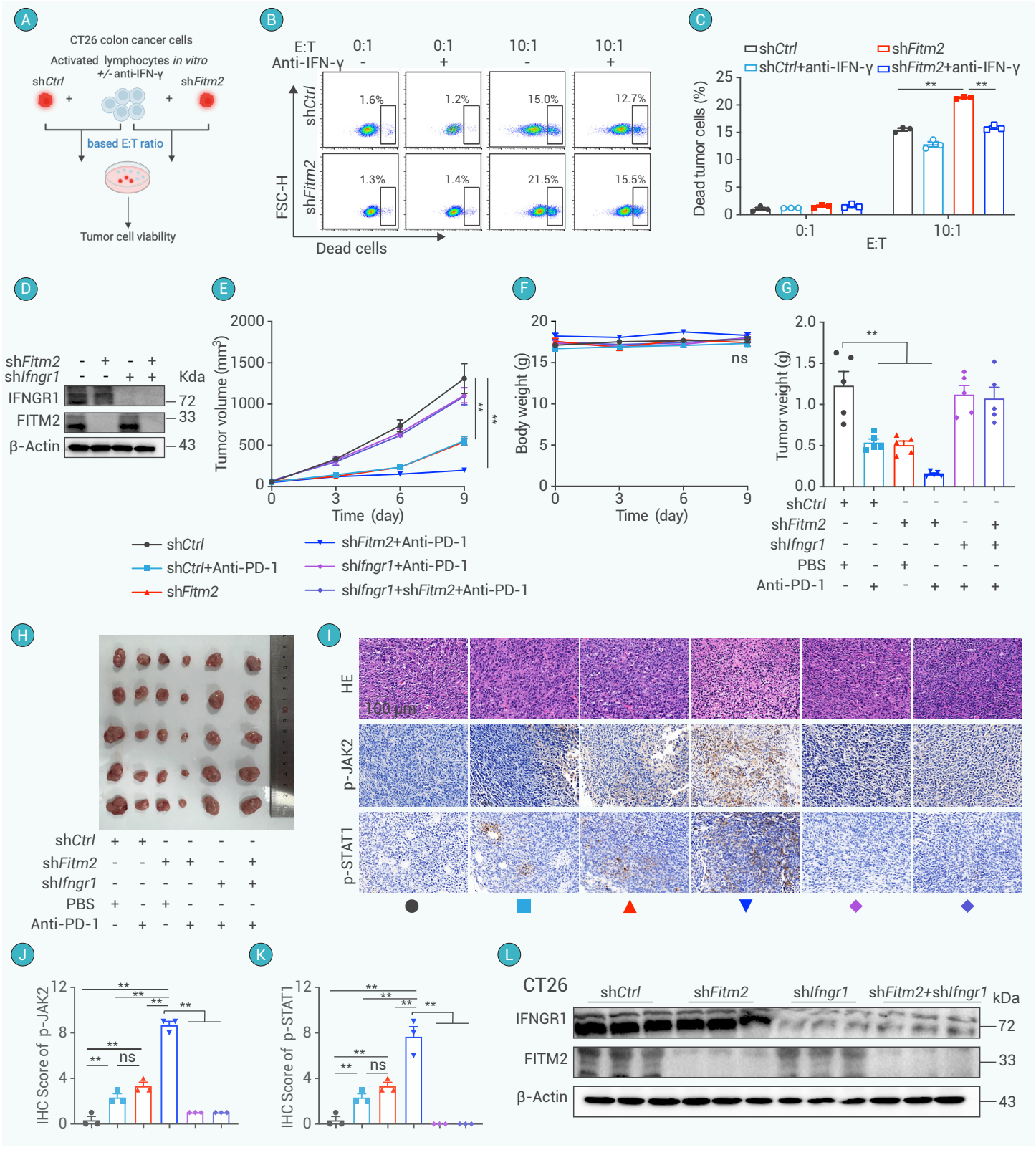


Figure 5. IFNGR1 signaling is essential for FITM2 knockdown to sensitize colorectal cancer to anti-PD-1 therapy (A-C) Cytotoxicity assay of CT26 sh*Ctrl* and sh*Fitm2* cells co-cultured with pre-activated mouse splenocytes, with or without IFN-γ neutralization antibody. (A) Schematic diagram of the *in vitro* co-culture system. (B, C) Flow cytometric analysis of target cell death at different effector-to-target (E: T) ratios in the absence or presence of anti-IFN-γ (20 μg/mL). (D) Validation of FITM2 and IFNGR1 knockdown in CT26 cells. (E-H) CT26 colon cancer cells (sh*Ctrl*, sh*Fitm2*, sh*Ifngr1*, and sh*Fitm2*+sh*Ifngr1*) were transplanted into BALB/c mice and treated with anti-PD-1 or PBS control. Shown are (E) tumor growth curves, (F) mouse body weight, (G) final tumor weight, and (H) representative tumor images. (I-K) Histological analysis of CT26 tumors: (I) H&E staining and IHC for (J) p-JAK2 and (K) p-STAT1. Scale bar, 100 μm. (L) Western blot validation of FITM2 and IFNGR1 knockdown efficiency in the CT26 tumors. Data were presented as means ± SEMs. ns, not significant; $^{**}P<0.01$, $^{*}P<0.05$.

(Figures 5I-K). These data demonstrate that the IFNGR1 surface expression and IFN-γ signaling are essential for FITM2 knockdown to sensitize colorectal cancer to anti-PD-1.

Pharmacological DGAT1 inhibition with A922500 restores TGN DAG, rescues IFNGR1 trafficking, and synergizes with anti-PD-1

Given that IFNGR1 membrane localization depends on DAG in the TGN, we

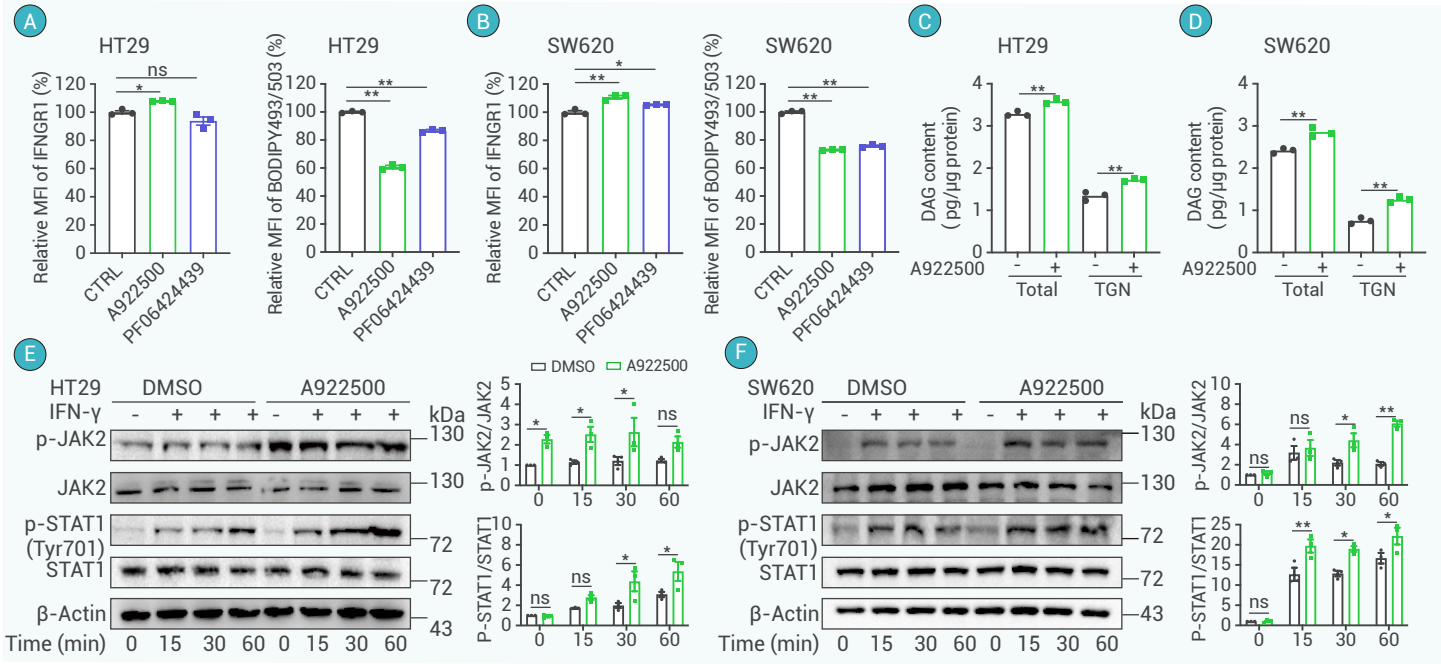


Figure 6. Pharmacological inhibition of lipid droplet biogenesis with DGAT1 inhibitor A922500 restores TGN DAG, rescues IFNGR1 trafficking and increases tumor-intrinsic IFN-γ-JAK2-STAT1 signaling (A, B) Flow cytometric analysis of IFNGR1 surface expression and neutral lipid content (BODIPY 493/503 MFI) in (A) HT29 and (B) SW620 colon cancer cells following a 24 h treatment with A922500 (10 μM), PF-06424439(10 μM) or DMSO control. (C, D) Measurement of DAG content in total cell lysates and TGN fractions from (C) HT29 and (D) SW620 cells treated with A922500 (10 μM) or DMSO for 24 h. (E, F) Western blot analysis of JAK2 and STAT1 phosphorylation in (E) HT29 and (F) SW620 cells pre-treated with A922500 or DMSO for 24 h, then stimulated with IFN-γ (10 ng/mL) for the indicated times.Data were presented as means ± SEMs. ns, not significant; $^{**}P$ <0.01, $^{*}P$ <0.05.

investigated whether pharmacologic inhibition of diacylglycerol acyltransferases (DGATs), which catalyze the final step of triacylglycerol synthesis, could replicate the effect of genetic FITM2 depletion *in vivo*. We assessed IFNGR1 surface expression and neutral lipid content in HT29 and SW620 cells treated with DGAT1 inhibitor A922500 or DGAT2 inhibitor PF-06424439. Treatment with the DGAT1 inhibitor A922500, but not the DGAT2 inhibitor, markedly reduced LD accumulation and significantly increased IFNGR1 expression on the plasma membrane in both cell lines (Figures 6A-B). Consistent with the genetic models, A922500 treatment restored DAG levels both globally and specifically within the TGN fractions (Figures 6C-D). Consequently, A922500 treatment enhanced IFN-γ-induced phosphorylation of JAK2 (Tyr1007/1008) and STAT1 (Tyr701) in both HT29 and SW620 cells (Figures 6E-F). Together, these findings pharmacologically corroborate our genetic models, establishing that restricting lipid droplet biogenesis, either via FITM2 silencing or DGAT1 inhibition, prevents Golgi diacylglycerol depletion and rescues IFNGR1 plasma membrane trafficking to restore tumor-intrinsic IFN-γ responsiveness.

Consistent with our genetic models, pharmacological inhibition of LD biogenesis with A922500 significantly sensitized orthotopic CT26 tumors to anti-PD-1 therapy, as evidenced by reduced bioluminescence intensity and tumor burden. In the orthotopic CT26 colon cancer model, the combination of A922500 with anti-PD-1 therapy markedly suppressed tumor growth (Figures 7A-D). H&E and PCNA staining further confirmed the anti-proliferative effect of the combination regimen (Figure 7E). Consistent with the *in vitro* findings, A922500 treatment reduced LD content and increased IFNGR1 expression on the plasma membrane of tumor cells *in vivo* (Figures 7F-G). Flow cytometry analysis of tumor-infiltrating lymphocytes revealed enhanced infiltration of $CD8^+$ and $CD4^+$ T cells, along with increased production of IFN-γ, TNF-α, and GZMB by $CD8^+$ T cells in the combination group (Figures 7H-L). Moreover, IHC staining of tumor tissues showed that the combination treatment significantly upregulated the level of p-JAK2 and p-STAT1 (Figures 7M-N). Importantly, this therapeutic strategy exhibited a favorable safety profile, as indicated by the absence of significant changes in serum ALT and AST levels (Figures S13A-B) and no histopathological alterations in major organs (Figure S13C).

Collectively, DGAT1 inhibition by A922500 reduces LD accumulation, restores IFNGR1 membrane trafficking, and enhances IFN-γ signaling, thereby potentiating the antitumor efficacy of anti-PD-1 immunotherapy in colorectal cancer.

DISCUSSION

Most CRC patients do not derive significant therapeutic benefits from ICIs. While LDs are known to contribute to various aspects of tumor biology, including tumor proliferation, invasion, metastasis, and resistance to chemoradiotherapy,[13,33-35] their role in modulating the efficacy of immunotherapy in CRC has remained controversial. Previous studies have shown that LDs serve as reservoirs of cyclooxygenase 2 (COX2) and sites for prostaglandin E2 (PGE2) synthesis in colon cancer cells, playing a crucial role in cell proliferation by participating in inflammatory processes.[36,37] Additionally, the acidic tumor microenvironment can promote autocrine TGF-β2 signaling, resulting in the accumulation of LDs and epithelial-to-mesenchymal transition. LD accumulation regulated by lipid droplet-localizing enzyme lysophosphatidylcholine acyltransferase 2 (LPCAT2) in colon cancer cells also confers resistance to chemotherapy by impairing caspase cascade activation and endoplasmic reticulum stress.[14] We identify a previously unrecognized immunoregulatory function of LDs, specifically those regulated by FITM2, in shaping the response to anti-PD-1 therapy in CRC. Unlike previous studies focusing on LD-associated enzymes or inflammatory mediators, we uncover a membrane trafficking-centered mechanism: FITM2-driven LDs modulate IFNGR1 plasma membrane localization through TGN DAG-dependent trafficking, thereby defining a metabolic checkpoint that governs tumor IFN-γ responsiveness in colorectal cancer.

Beyond the CRC context, our findings contribute to an emerging picture in which LDs serve as immunoregulatory organelles that integrate cellular metabolism with immune signaling across diverse biological settings. Bosch et al. recently demonstrated that LDs function as innate immune hubs in macrophages, where they compartmentalize antimicrobial proteins and eicosanoid biosynthetic enzymes to mediate host defense.[21] More broadly, LDs have been implicated in the regulation of antigen cross-presentation in dendritic cells, the metabolic reprogramming of tumor-associated macrophages, and the effector function of $CD8^+$ T cells within the tumor microenvironment.[38,39] Our discovery that LDs control cytokine receptor trafficking through organelle-specific DAG partitioning adds a new dimension to this paradigm: beyond their established roles as platforms for protein

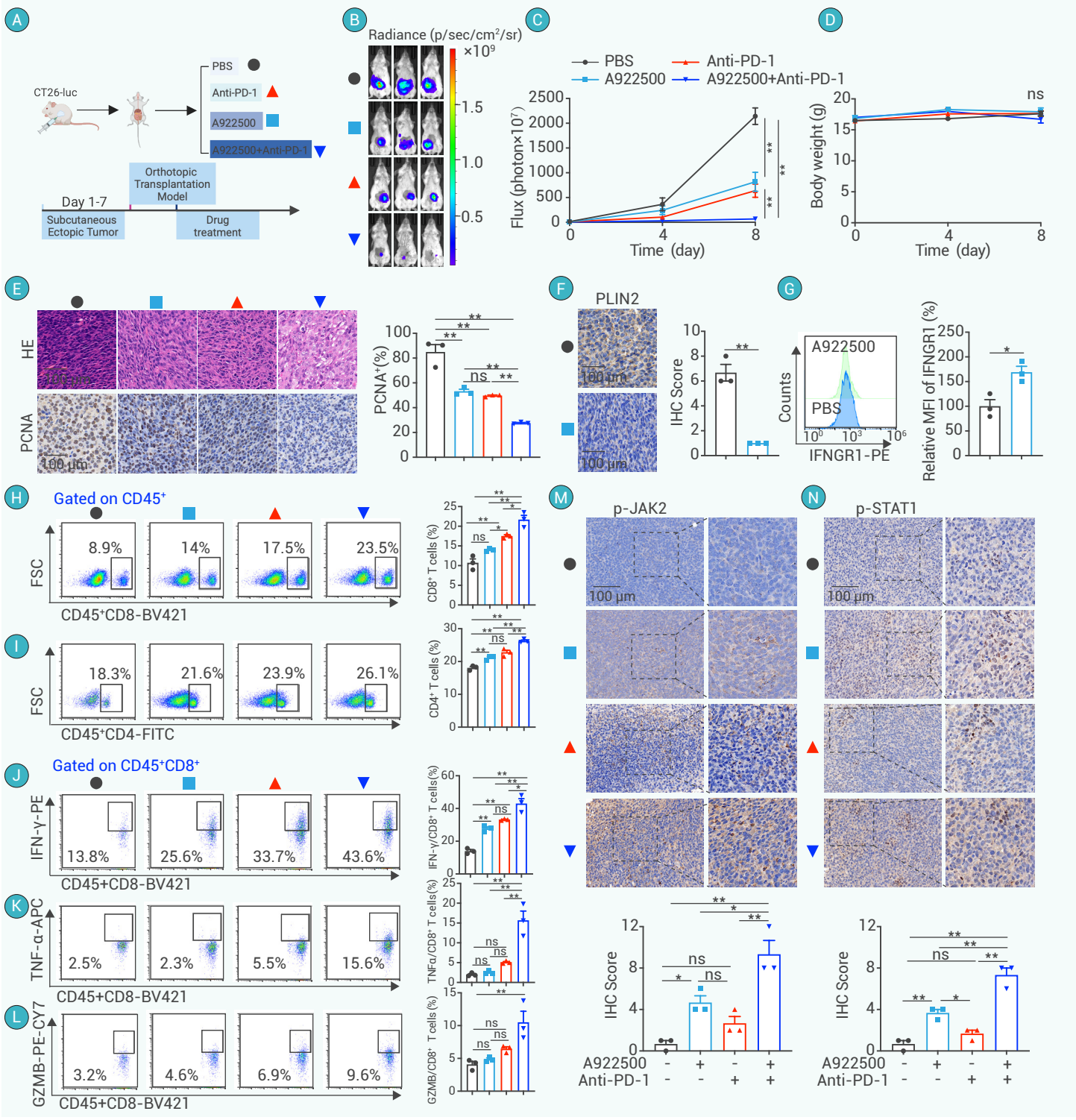


Figure 7. Pharmacological inhibition of lipid droplet biogenesis with DGAT1 inhibitor A922500 synergizes with anti-PD-1 therapy (A) Schematic diagram of the experimental timeline. (B) Bioluminescence images of orthotopic tumors. (C) Quantification of tumor burden from bioluminescence data. (D) Mouse body weight curves throughout the study. (E) Representative images of tumor sections stained with H&E and for the proliferation marker PCNA. Scale bar, 100 μm. (F) IHC for the lipid droplet marker PLIN2 in tumor tissues. Scale bar, 100 μm. (G) Flow cytometric analysis of IFNGR1 surface expression on $CD45^-$ tumor cells isolated from A922500- or PBS-treated tumors. (H, I) Proportion of tumor-infiltrating (H) $CD8^+$ T cells and (I) $CD4^+$ T cells among $CD45^+$ leukocytes, as determined by flow cytometry. (J-L) Intracellular cytokine staining and flow cytometry analysis of tumor-infiltrating $CD8^+$ T cells to produce (J) IFN-γ, (K) TNF-α, and (L) GZMB. (M, N) IHC analysis of phosphorylated signaling molecules in tumor tissues: (M) p-JAK2 and (N) p-STAT1. Scale bar, 100 μm. Data were presented as means ± SEMs. ns, not significant; $^{**}P<0.01$, $^{*}P<0.05$.

sequestration and eicosanoid production, LDs can actively reshape the plasma membrane receptor landscape by regulating lipid flux to the secretory pathway.

An important question arising from our study is whether LD biogenesis selectively impacts IFNGR1 or globally alters the surface expression of multiple receptors. Our unbiased quantitative cell surface proteomics (Figures 2I-L) revealed that FITM2 depletion indeed alters the abundance of several plasma membrane proteins beyond IFNGR1. Beyond IFNGR1, this LD-TGN regulatory axis may function as a general gatekeeper for other Golgi-dependent surface receptors. Although other receptors showed altered surface abundance in the proteomic screen, none of the corresponding downstream signaling pathways (e.g., TNF, IL-6, or growth factor pathways) were signifi-

cantly enriched in our RNA-seq or phospho-proteomic analyses following FITM2 modulation. Second, the functional rescue of anti-PD-1 efficacy by LD reduction was completely abrogated by IFNGR1 knockdown or IFN-γ neutralization (Figure 5), placing IFNGR1 as a non-redundant effector. Third, the trafficking defect induced by LD accumulation is specifically rescued by replenishing TGN DAG via DGAT1 inhibition, which restores IFNGR1 surface expression but does not globally correct all proteomic changes. Moreover, the LD-TGN axis identified here may operate in other pathological contexts characterized by aberrant LD accumulation, including metabolic dysfunction-associated steatohepatitis (MASH), obesity-associated cancer risk, and chronic infection, where modulated receptor presentation and downstream signaling, given that altered lipid metabolism intersects with immune surveillance.

However, the critical finding is that under IFN-γ stimulation—the specific context of anti-tumor immunity—the functional converges on the IFNGR1-JAK2-STAT1 axis. Several lines of evidence support this selectivity. We proposed a model where LD-mediated TGN DAG depletion creates a general vulnerability in secretory trafficking, but the physiological consequence is dictated by the cytokine context. In the tumor microenvironment, where IFN-γ is a dominant effector molecule, the impaired trafficking of IFNGR1 becomes a rate-limiting event for anti-tumor immunity. Thus, while LDs may influence multiple receptors, their immunoregulatory function is selective for the IFN-γ pathway.

The canonical IFN-γ signaling pathway plays a critical role in the response to various immunotherapies, including ICIs and chimeric antigen receptor (CAR) T-cell therapy.[40] Disruption of this pathway, through mutations in B2M, JAK1/2, or IFNGR1/2, can cause loss of MHC-I expression or IFN-γ unresponsiveness, leading to resistance to ICIs.[41-43] Other regulators such as PTPN2 (a JAK/STAT phosphatase) and ADAR1 (an RNA-editing enzyme modulating ISG expression) also shape tumor immune sensitivity.[44,45] In addition to IFNGR1 expression levels, its subcellular localization is critical for IFN-γ signal transduction.[2] Genome-wide CRISPR screens have identified IFNGR1 as a determinant of CAR-T efficacy in solid tumors,[46] and loss of IFNGR1 confers resistance to anti-PD-1 therapy in MC38 colon cancer cells.[47] Mechanisms such as ubiquitin ligase STUB1-mediated degradation, optineurin loss, or altered N-glycosylation can similarly impair IFNGR1 stability.[2,48,49] In our study, FITM2 depletion increased IFNGR1 surface expression without affecting total protein abundance, correlating with enhanced response to anti-PD-1 treatment. This mechanism is distinct from previously reported regulators of IFNGR1, expanding the known mechanisms governing cytokine receptor availability. This finding also parallels a recent report that glycosphingolipid depletion increases IFNGR1 surface availability;[50] however, we provide a distinct mechanistic basis (TGN DAG depletion) and identify LD biogenesis as an upstream, druggable regulator.

To further elucidate the mechanism underlying IFNGR1 localization changes, we examined its biosynthesis and trafficking pathway. IFNGR1 is synthesized in the endoplasmic reticulum and undergoes glycosylation during its transfer to the Golgi apparatus, with only fully glycosylated receptors reaching the plasma membrane.[28,51] Western blot analysis showed that FITM2 modulation did not alter IFNGR1 glycosylation (no molecular weight shift) and CHX chase assays confirmed that FITM2 does not affect IFNGR1 synthesis or degradation. Additionally, we found that a fraction of IFNGR1 localized to the TGN, and LD depletion *via* FITM2 knockdown promoted IFNGR1 trafficking to the plasma membrane. Prior studies demonstrated that Nir2-mediated DAG homeostasis in the Golgi is essential for vesicular export.[32] Our results establish a trafficking-centered mechanism in which LD abundance modulates TGN DAG pools to control IFNGR1 surface availability and downstream IFN-γ signaling.

Building on this mechanism, we identified that the DGAT1 inhibitor A922500, which effectively reduces LDs, restores TGN DAG levels, and sensitizes CRC to anti-PD-1 therapy. The agent exhibited robust antitumor efficacy *in vivo* with no significant changes in body weight or histopathological abnormalities in major organs. DGAT1 inhibition has shown antitumor effects in multiple cancer types, with gastrointestinal events being the primary adverse effects.[52] In preclinical settings, DGAT1 inhibitors did not affect body weight, consistent with our findings.[24,53] Importantly, the favorable safety profile and the ongoing clinical trials of DGAT1 inhibitors for metabolic diseases support their repurposing for cancer immunotherapy.[54]

A limitation of our study is that the *in vivo* efficacy was evaluated in immune-competent mouse models with established CRC cell lines; further validation in patient-derived xenograft (PDX) or genetically engineered mouse models is needed. While we focus on FITM2 as a tool to manipulate LDs, other LD-regulatory pathways may have distinct effects on membrane trafficking and could be explored in future studies. Additionally, future studies using DGAT1-KO cells or intestine-restricted DGAT1 inhibitors will further refine mechanistic specificity.

CONCLUSION

In summary, the study uncovers a previously unappreciated immunosuppressive role of LDs in CRC. FITM2-driven LD biogenesis depletes TGN DAG pools, impeding IFNGR1 trafficking and attenuating IFN-γ signaling. Conversely, LD reduction via genetic or pharmacological intervention restores IFNGR1 surface localization and enhances responsiveness to anti-PD-1 therapy. Our findings redefine LDs as active immunoregulatory organelles rather than passive lipid reservoirs and highlight the therapeutic potential of targeting LD biogenesis and TGN lipid homeostasis to improve immunotherapy outcomes in CRC.

REFERENCES

1. Dekker E., Tanis P.J., Vleugels J.L.A., et al. (2019). Colorectal cancer. *Lancet* **394**:1467–1480. DOI:10.1016/S0140-6736(19)32319-0
2. Apriamashvili G., Vredevoogd D.W., Krijgsman O., et al. (2022). Ubiquitin ligase STUB1 destabilizes IFNγ-receptor complex to suppress tumor IFNgamma signaling. *Nat. Commun.* **13**:1923. DOI:10.1038/s41467-022-29442-x
3. Lizardo D.Y., Kuang C., Hao S., et al. (2020). Immunotherapy efficacy on mismatch repair-deficient colorectal cancer: From bench to bedside. *Biochim. Biophys. Acta Rev. Cancer* **1874**:188447. DOI:10.1016/j.bbcan.2020.188447
4. Pecci F., Cantini L., Bittoni A., et al. (2021). Beyond microsatellite instability: Evolving strategies integrating immunotherapy for microsatellite stable colorectal cancer. *Curr. Treat. Options Oncol.* **22**:69. DOI:10.1007/s11864-021-00870-z
5. Baraibar I., Mirallas O., Saoudi N., et al. (2021). Combined treatment with immunotherapy-based strategies for MSS metastatic colorectal cancer. *Cancers (Basel)* **13**:6311. DOI:10.3390/cancers13246311
6. Ganesh K., Stadler Z.K., Cercek A., et al. (2019). Immunotherapy in colorectal cancer: Rationale, challenges and potential. *Nat. Rev. Gastroenterol. Hepatol.* **16**:361–375. DOI:10.1038/s41575-019-0126-x
7. Wang C. and Fakih M. (2021). Targeting MSS colorectal cancer with immunotherapy: Are we turning the corner. *Expert Opin. Biol. Ther.* **21**:1347–1357. DOI:10.1080/14712598. 2021.1 933940.
8. Schoenfeld A.J. and Hellmann M.D. (2020). Acquired resistance to immune checkpoint inhibitors. *Cancer Cell* **37**:443–455. DOI:10.1016/j.ccell.2020.03.017
9. Bagchi S., Yuan R. and Engleman E.G. (2021). Immune checkpoint inhibitors for the treatment of cancer: Clinical impact and mechanisms of response and resistance. *Annu. Rev. Pathol.* **16**:223–249. DOI:10.1146/annurev-pathol-042020-042741
10. Kim T.K., Vandsemb E.N., Herbst R.S., et al. (2022). Adaptive immune resistance at the tumour site: Mechanisms and therapeutic opportunities. *Nat. Rev. Drug Discov.* **21**:529–540. DOI:10.1038/s41573-022-00493-5
11. Kalbasi A. and Ribas A. (2020). Tumour-intrinsic resistance to immune checkpoint blockade. *Nat. Rev. Immunol.* **20**:25–39. DOI:10.1038/s41577-019-0218-4
12. Olzmann J.A. and Carvalho P. (2019). Dynamics and functions of lipid droplets. *Nat. Rev. Mol. Cell Biol.* **20**:137–155. DOI:10.1038/s41580-018-0085-z
13. Li Z., Liu H. and Luo X. (2020). Lipid droplet and its implication in cancer progression. *Am. J. Cancer Res* **10**:4112–4122.
14. Cotte A.K., Aires V., Fredon M., et al. (2018). Lysophosphatidylcholine acyltransferase 2-mediated lipid droplet production supports colorectal cancer chemoresistance. *Nat. Commun.* **9**:322. DOI:10.1038/s41467-017-02732-5
15. Kasashima H., Duran A., Cid-Diaz T., et al. (2021). Mouse model of colorectal cancer: Orthotopic co-implantation of tumor and stroma cells in cecum and rectum. *STAR Protoc.* **2**:100297. DOI:10.1016/j.xpro.2021.100297
16. Campion C.G., Zaoui K., Verissimo T., et al. (2018). COMMD5/HCaRG Hooks endosomes on cytoskeleton and coordinates EGFR trafficking. *Cell Rep.* **24**:670–684e677. DOI:10.1016/j.celrep.2018.06.056
17. Wei B., Xu L., Guo W., et al. (2021). SHP2-mediated inhibition of DNA repair contributes to cGAS-STING activation and chemotherapeutic sensitivity in colon cancer. *Cancer Res.* **81**:3215–3228. DOI:10.1158/0008-5472.CAN-20-3738
18. Hu J., Liu W., Zou Y., et al. (2024). Allosterically activating SHP2 by oleanolic acid inhibits STAT3-Th17 axis for ameliorating colitis. *Acta Pharm. Sin. B* **14**:2598–2612. DOI:10.1016/j.apsb.2024.03.017
19. Bacci M., Lorito N., Smiriglia A., et al. (2024). Acetyl-CoA carboxylase 1 controls a lipid droplet-peroxisome axis and is a vulnerability of endocrine-resistant ER(+) breast cancer. *Sci. Transl. Med.* **16**:eadf9874. DOI:10.1126/scitranslmed.adf9874
20. Liu R., Lee J.H., Li J., et al. (2021). Choline kinase alpha 2 acts as a protein kinase to

promote lipolysis of lipid droplets. *Mol. Cell* **81**:2722-2735.e9. DOI:10.1016/j.molcel.2021.05.005
21. Bosch M., Sanchez-Alvarez M., Fajardo A., et al. (2020). Mammalian lipid droplets are innate immune hubs integrating cell metabolism and host defense. *Science* **370**:eaay8085. DOI:10.1126/science.aay8085
22. Lyu X., Wang J., Wang J., et al. (2021). A gel-like condensation of Cidec generates lipid-permeable plates for lipid droplet fusion. *Dev. Cell* **56**:2592-2606.e7. DOI:10.1016/j.devcel.2021.08.015.
23. Kadereit B., Kumar P., Wang W.J., et al. (2008). Evolutionarily conserved gene family important for fat storage. *Proc. Natl. Acad. Sci. USA* **105**:94–99. DOI:10.1073/pnas.0708579105
24. Cheng X., Geng F., Pan M., et al. (2020). Targeting DGAT1 ameliorates glioblastoma by increasing fat catabolism and oxidative stress. *Cell Metab.* **32**:229–242.e8. DOI:10.1016/j.cmet.2020.06.002
25. Zhou L., Song Z., Hu J., et al. (2021). ACSS3 represses prostate cancer progression through downregulating lipid droplet-associated protein PLIN3. *Theranostics* **11**:841–860. DOI:10.7150/thno.49384
26. Gao M., Huang X., Song B.L., et al. (2019). The biogenesis of lipid droplets: Lipids take center stage. *Prog Lipid Res.* **75**:100989. DOI:10.1016/j.plipres.2019.100989
27. Zaidi M.R. and Merlino G. (2011). The two faces of interferon-γ in cancer. *Clin. Cancer Res.* **17**:6118–6124. DOI:10.1158/1078-0432.CCR-11-0482
28. Londino J.D., Gulick D.L., Lear T.B., et al. (2017). Post-translational modification of the interferon-gamma receptor alters its stability and signaling. *Biochem. J.* **474**:3543–3557. DOI:10.1042/BCJ20170548
29. Krahmer N., Najafi B., Schueder F., et al. (2018). Organellar proteomics and phospho-proteomics reveal subcellular reorganization in diet-induced hepatic steatosis. *Dev. Cell* **47**:205-221.e7. DOI:10.1016/j.devcel.2018.09.017.
30. Xu M., Chen Z.Y., Li Y., et al. (2024). Rab2A-mediated Golgi-lipid droplet interactions support very-low-density lipoprotein secretion in hepatocytes. *EMBO J* **43**:6383–6409. DOI:10.1038/s44318-024-00288-x
31. Gu F., Crump C.M. and Thomas G. (2001). Trans-Golgi network sorting. *Cell Mol. Life Sci.* **58**:1067–1084. DOI:10.1007/PL00000922
32. Litvak V., Dahan N., Ramachandran S., et al. (2005). Maintenance of the diacylglycerol level in the Golgi apparatus by the Nir2 protein is critical for Golgi secretory function. *Nat. Cell. Biol.* **7**:225–234. DOI:10.1038/ncb1221
33. Corbet C., Bastien E., Santiago de Jesus J.P., et al. (2020). TGFbeta2-induced formation of lipid droplets supports acidosis-driven EMT and the metastatic spreading of cancer cells. *Nat. Commun.* **11**:454. DOI:10.1038/s41467-019-14262-3
34. Wright H.J., Hou J., Xu B., et al. (2017). CDCP1 drives triple-negative breast cancer metastasis through reduction of lipid-droplet abundance and stimulation of fatty acid oxidation. *Proc. Natl. Acad. Sci. USA* **114**:E6556–E6565. DOI:10.1073/pnas.1703791114
35. Luis G., Godfroid A., Nishiumi S., et al. (2021). Tumor resistance to ferroptosis driven by Stearoyl-CoA Desaturase-1 (SCD1) in cancer cells and fatty acid biding protein-4 (FABP4) in tumor microenvironment promote tumor recurrence. *Redox. Biol.* **43**:102006. DOI:10.1016/j.redox.2021.102006
36. Accioly M.T., Pacheco P., Maya-Monteiro C.M., et al. (2008). Lipid bodies are reservoirs of cyclooxygenase-2 and sites of prostaglandin-E2 synthesis in colon cancer cells. *Cancer Res.* **68**:1732–1740. DOI:10.1158/0008-5472.CAN-07-1999
37. Zheng M., Zhang W., Chen X., et al. (2023). The impact of lipids on the cancer-immunity cycle and strategies for modulating lipid metabolism to improve cancer immunotherapy. *Acta Pharm. Sin. B* **13**:1488–1497. DOI:10.1016/j.apsb.2022.10.027
38. Niu Z., Chen G., Chang W., et al. (2021). Chimeric antigen receptor-modified macrophages trigger systemic anti-tumour immunity. *J. Pathol.* **253**:247–257. DOI:10.1002/path.5585
39. Siddiqui S. and Glauben R. (2022). Fatty acid metabolism in myeloid-derived suppressor cells and tumor-associated macrophages: Key factor in cancer immune evasion. *Cancers (Basel)* **14**:250. DOI:10.3390/cancers14010250
40. Ayers M., Lunceford J., Nebozhyn M., et al. (2017). IFN-gamma-related mRNA profile predicts clinical response to PD-1 blockade. *J. Clin. Invest.* **127**:2930–2940. DOI:10.1172/JCI91190
41. Zaretsky J.M., Garcia-Diaz A., Shin D.S., et al. (2016). Mutations associated with acquired resistance to PD-1 blockade in melanoma. *N. Engl. J. Med.* **375**:819–829. DOI:10.1056/NEJMoa1604958
42. Shin D.S., Zaretsky J.M., Escuin-Ordinas H., et al. (2017). Primary resistance to PD-1 Blockade mediated by JAK1/2 mutations. *Cancer Discov.* **7**:188–201. DOI:10.1158/2159-8290.CD-16-1223
43. Gao J., Shi L.Z., Zhao H., et al. (2016). Loss of IFN-gamma pathway genes in tumor cells as a mechanism of resistance to anti-CTLA-4 therapy. *Cell* **167**:397–404.e9. DOI:10.1016/j.cell.2016.08.069
44. Manguso R.T., Pope H.W., Zimmer M.D., et al. (2017). In vivo CRISPR screening identifies Ptpn2 as a cancer immunotherapy target. *Nature* **547**:413–418. DOI:10.1038/nature23270
45. Ishizuka J.J., Manguso R.T., Cheruiyot C.K., et al. (2019). Loss of ADAR1 in tumours overcomes resistance to immune checkpoint blockade. *Nature* **565**:43–48. DOI:10.1038/s41586-018-0768-9
46. Larson R.C., Kann M.C., Bailey S.R., et al. (2022). CAR T cell killing requires the IFNgammaR pathway in solid but not liquid tumours. *Nature* **604**:563–570. DOI:10.1038/s41586-022-04585-5
47. Lv C., Yuan D. and Cao Y. (2021). Downregulation of interferon-gamma receptor expression endows resistance to anti-programmed death protein 1 therapy in colorectal cancer. *J. Pharmacol. Exp. Ther.* **376**:21–28. DOI:10.1124/jpet.120.000284
48. Du W., Hua F., Li X., et al. (2021). Loss of optineurin drives cancer immune evasion via palmitoylation-dependent IFNGR1 lysosomal sorting and degradation. *Cancer Discov.* **11**:1826–1843. DOI:10.1158/2159-8290.CD-20-1571
49. Krug J., Rodrian G., Petter K., et al. (2023). N-glycosylation regulates intrinsic IFN-γ resistance in colorectal cancer: Implications for immunotherapy. *Gastroenterology* **164**:392-406.e5. DOI:10.1053/j.gastro.2022.11.018
50. Soula M., Unlu G., Welch R., et al. (2024). Glycosphingolipid synthesis mediates immune evasion in KRAS-driven cancer. *Nature* **633**:451–458. DOI:10.1038/s41586-024-07787-1
51. Pestka S., Kotenko S.V., Muthukumaran G., et al. (1997). The interferon gamma (IFN-gamma) receptor: A paradigm for the multichain cytokine receptor. *Cytokine Growth Factor Rev.* **8**:189–206. DOI:10.1016/s1359-6101(97)00009-9
52. Deng B., Kong W., Shen X., et al. (2024). The role of DGAT1 and DGAT2 in regulating tumor cell growth and their potential clinical implications. *J. Transl. Med.* **22**:290. DOI:10.1186/s12967-024-05084-z
53. Dierge E., Debock E., Guilbaud C., et al. (2021). Peroxidation of n-3 and n-6 polyunsaturated fatty acids in the acidic tumor environment leads to ferroptosis-mediated anticancer effects. *Cell Metab.* **33**:1701-1715.e5. DOI:10.1016/j.cmet.2021.05.016
54. Wang L.S., Xu S.W., Zhou M.Z., et al. (2024). The role of DGAT1 and DGAT2 in tumor progression via fatty acid metabolism: A comprehensive review. *Int. J. Biol. Macromol.* **278:134835**. DOI:10.1016/j.ijbiomac.2024.134835

FUNDING AND ACKNOWLEDGMENTS

This work was supported by National Natural Science Foundation of China (82273197, 82403832, 82273933), Key project of Science and Technology in Jiangsu Province (BG2024007). The funders had no role in study design, data collection and analysis, decision to publish, or preparation of the manuscript.

AUTHOR CONTRIBUTIONS

Xu LY, Gu YH, Guo WJ and Xu Q conceptually designed the study. Xu LY, Li XF and Li YF performed the majority experiments. Tang ZH, Huang K and Song WC performed the animal experiments. Jiang W and Han X participated in the collection of clinical samples. Xu LY, Li YF and Guo WJ wrote and revised the manuscript and revisions based on feedback from all co-authors. All authors reviewed the results and approved the final version of the manuscript.

DECLARATION OF INTERESTS

The authors declare no competing interests.

ETHICAL STATEMENT AND PATIENT CONSENT

This study was approved by the Ethics Committee of Nanjing Medical University, with efforts to reduce animal members and minimize suffering (Nanjing, P.R. China; IACUC-2410055) and the Ethics Commission of Jiangsu Province Hospital (2021-SR-160.A1 and 2021-SR-544).

DATA AND CODE AVAILABILITY

All data supporting the findings of this study are available in the article. The paper does not contain original code. The RNA-seq data generated in this study have been deposited in the NCBI Gene Expression Omnibus (GEO) under the accession number: GSE289818. The mass spectrometry proteomics data have been publicly released via the iProX partner repository with the identifier IPX0014070000.

SUPPLEMENTAL INFORMATION

It can be found online at https://doi.org/10.59717/j.xinn-oncol.2026.100041